UNIVERSIDAD POLITÉCNICA DE CARTAGENA

FINAL PROJECT

Analysis of dry friction by friction test bench

Author:
Antonio MIRALLES PÉREZ

Supervisors:
Dr. José Andrés MORENO NICOLÁS
Dr. Fulgencio MARÍN GARCÍA

Contents

List of Figures

1 Introduction

1.1 Introduction

The subject of this work is the analysis of a frictional dry process; to be precise in a simplified model, Figure 2, of a Girling duo-servo brake mechanism, Figure 1.

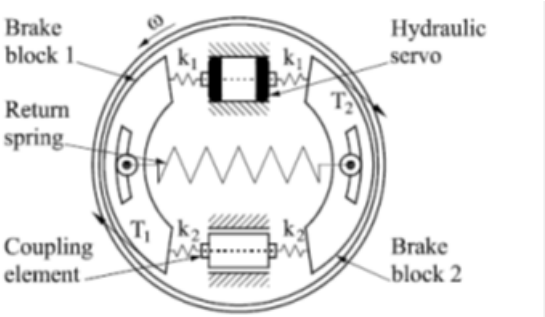

Figure 1: Girling duo-servo brake mechanism

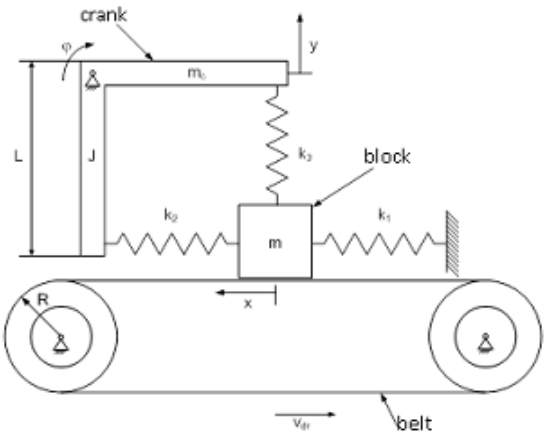

Figure 2: Simplification of a Girling duo-servo brake mechanism

The electric engine drives the wheel which produces the belt's motion. The engine operates at different velocities, with the geometry of the system and the value of the operation velocity, belt's speed can be assessed. Sensitivity of the measuring probe and latter velocity are linked with each other at stick phase.

1.2 State of the science

Dry friction is one of the most fundamentals working fields in mechanical engineering, several works has been developed related to this phenomenon. Despite of the quotidian and the long history in this working field, its analysis has been

showing some difficulties. On the one hand, any work related with dry friction, an apparently macroscopic phenomenon, must be analyzed also in a microscopic scale. On the other hand, the process shows a radically different behaviour in static and dynamic conditions, the parameters used to represent the results of this kind of analysis are also different. In static conditions, the main objective is to assess the force required to begin the motion, while in dynamic conditions the most important interest is to know the speed about the friction force stabilizes and reach its minimum value. Moreover, the solution to static and dynamic problems is so sensitive to the value range of the parameters which define the system. Consequentially, the way of the motion in both cases shows qualitative differences between them and the global friction force takes a wide range of values.

Historically, the first try to explain the Colulomb laws in an atomic way is attributed to Tomlinson (Tomlinson 1929). This author supposed that the atoms of a surface act as uncoupled oscillators respect atoms belonged to the other surface, as fingers playing the guitar-strings to make it sounds. Beyond the hook, the atoms jump in an abrupt way between two equilibrium positions. Afterwards, Frenkel-Kontorova model considered the coupling between atoms (Frenkel and Kontorova 1938): a one-dimensional model in which chained atoms are absorbed, lineally coupled and interacted with the fixed surface by a potential, periodic in space.

The combination of latter models points to Frenkel-Kontorova-Tomlinson model (FKT model), Figure 3. This model (Weiss & Elmer 1996; Weiss & Elmer 1997; Alhama, Marn et al. 2011) considers the coupling between atoms of the surface belonged to the slipping block, not considered by Tomlinson, and between each atoms and the inside of the slipping block neither considered by Frenkel and Kontorova.

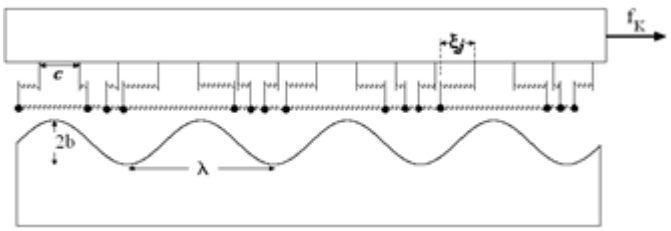

Figure 3: Physical representation of FKT model

Despite of the apparently simplicity of the latter models, dry friction shows sometimes surprising behaviours, like important changes in the friction coefficient, being potentially useful in mechanics designs. To be precise, for static friction Aubry showed that an almost infinitesimal force can produce displacement if the value of the periodic potential is under a critic value, analyticity rupture, and the ratio between constant of the crystal network in a surface, and the other one in the other surface is an irrational number (Aubry 1979).

When slipping occurs, systems can show steady and even chaotic behaviours.

Other variants of FKT model have been applied to simulate microscopes which use a nanometric pointer on a smooth surface in an atomic level (Schwarz & Hlscher 2001). These microscopes are fundamental to understand in a much complete way how the dry friction works (Schwarz & Hlscher 2001).

The Scanning Force Microscope (SFM) allows studying friction with high accuracy in function of the contact geometry, the load applied, the effective contact area, the slipping speed and the structure of the surface that's being studied. With the use of this tool, it has been found some phenomenon in a nanometric scale that shows a similar behaviour to macroscopic scale friction, while others show a very different behaviour. Moreover, nanometric scale friction is proportional to the contact area, in difference whit macroscopic case. Also is difficult to ignore the independence between contact average pressure and shear stress.

A lot of issues have shown the sensitiveness of friction to little changes in the surface structure. Moreover, latters show the dependence between the crystal network and the angle of the slipping direction. This feature has been used several times to identify different areas in a chemist way, in the case of a sample originated by structural defects, but it couldn't be used to explain the fact that some surfaces have more tendency to friction than others.

Theoretical models of these microscopes have shown an usual stick-slip motion of the atoms belonged to the pointer on the surface of the sample, jumping from a minimum interaction potential pointer-sample to the next ones. Its paths are often similar to a zigzag curve which mission is to don't allow the atoms to take position on a region related to an atom of the sample associated with a maximum potential interaction. Because of latter specific behaviour, pictures of scanning force microscope shows only the periodicity of the minimum values of interaction potential, which in a general way doesn't match exactly with atomic structure of a sample of non-trivial crystal structure.

From the results of different issues it seems possible to obtain the Amontons and Coulomb friction laws from macroscopic effects. Greenwood (Greenwood & Williamson 1966; Greenwood 1992) showed that efficient contact area between macroscopically flat bodies, which however have a statistic roughness in a microscopic level, increases lineally with the load being applied, which delete any contradiction between the macroscopic and microscopic friction laws. Anyway, relative independence between friction force and slipping speed, even in a macroscopic or nanoscopic way could be explained through stick-slip motion of atoms due to the interaction potential between the pointer and the sample. If the relative velocity between the bodies is much lower than slipping velocity of the atoms, the dissipated energy will be independent of the slipping velocity variations.

Despite of all the researches, there are still questions without answers which are greater in number than questions being already answered. For example, is

still impossible to predict friction properties of a specific contact, even though the optimization of these surface properties of specific use is gaining relevance with the tendency of miniaturize mechanical systems.

From a practical point of view, surfaces being used in engineering can't be considered atomically smooth, which also requires a macroscopic level studies (Awrejcewicz & Olejnik 2005).

Other tool used to analyze friction phenomenon is the classic Burridge-Knopoff model (Burride & Knopoff 1967). Latter consist in a differential equation system used for simulation of earthquakes discretizing the problem using blocks system, where each one has mass'm'. These masses, which interact mutually beyond springs, are subjected to friction forces that depends on the velocity, $F_f(v_i)$, and interact with the ground elastically, Figure 4 (Cartwright, Hernández-Garcá et al. 1997). The motion equation is:

$$m \cdot \ddot{x_i} = k_c \cdot (x_{i+1} - 2x_i + x_{i-1}) - k_p \cdot (x_i - v \cdot t) - F_f(\dot{x_i}) \tag{1}$$

where k_c is the elastic constant of the spring that represents the interaction between masses, k_p is the elastic constant roles the play of the interaction between the masses and the ground and x_i is the deviation of the instant block position related to its equilibrium position. Carlson and Langer consider the fact that the friction force decrease asymptotically with the velocity, v, while blocks are moving in a stick-slip motion (Carlson & Langer 1989), Figure 4.

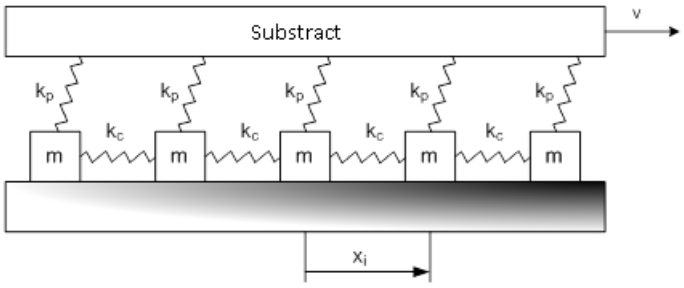

Figure 4: Burridge-Knopoff's model physical representation

The same stick-slip phenomenon associated with friction, descripted in Burridge-Knopoff model, is in the paper of Awrejcewicz and col. (Galvanetto & Bishop 1995; van de Vrande, van Campen et al. 1999; Galvanetto 2001; Galvanetto 2002; Awrejcewicz & Olejnik 2003 (3)). When the latter system is simplified, using only two masses, Figure 5, it is possible to understand better the dynamics of the process.

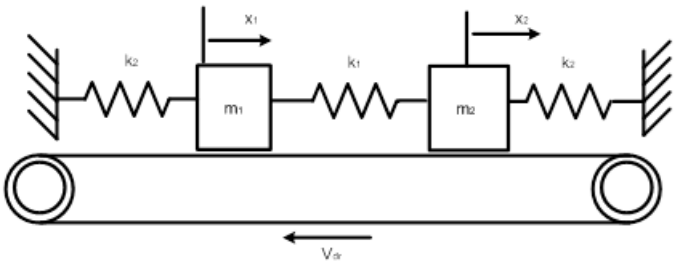

Figure 5: Burridge-Knopoff's model with two masses

The introduction of the dependence between friction forces and velocity of the model, allows to take account the bifurcations of the solution.

1.2.1 Influence of roughness on the dry friction coefficient

Superficial roughness is a factor with a great influence on the behaviour of dry contacts highly loaded (Mihailidis, Bakolas et al. 2001). The characterization of the rough surfaces is a really recognized problem in knowledge fields like science and technology (Thomas 1999). The general point of view for this characterization is based on several statistical parameters obtained from the superficial 3D map. In this way, some national general rules for the bi-dimensional characterization are R_a, R_z, S, and S_m. However these parameters are so general to characterize a tri-dimensional phenomenon, using them can produce the loss of important information about the organization of the surface (Myshkin, Grigoriev et al. 2003).

The improve on the accuracy of the profilometer, the traditional contact techniques, and also the non-contact ones, have allowed the roughness test in a nanometric scale, Figure 6 (Myshkin, Grigoriev et al. 2004). The last figure contains the comparison between the characteristics of the next measurement instruments:

- Scanning electronic microscope (SEM)
- Atomic force microscope (AFM)
- Tunnel effect microscope (STM)

Despite of the wide use associated with scanning probe microscope in surface studies, the measure of average parameters in a nanoscopic scale requires greater researches. It's difficult to compare surfaces taking account this problem, also to identify what role plays roughness on smooth surfaces during dry friction and to model mathematically contact phenomenon (Myshkin, Grigoriev et al. 2003).

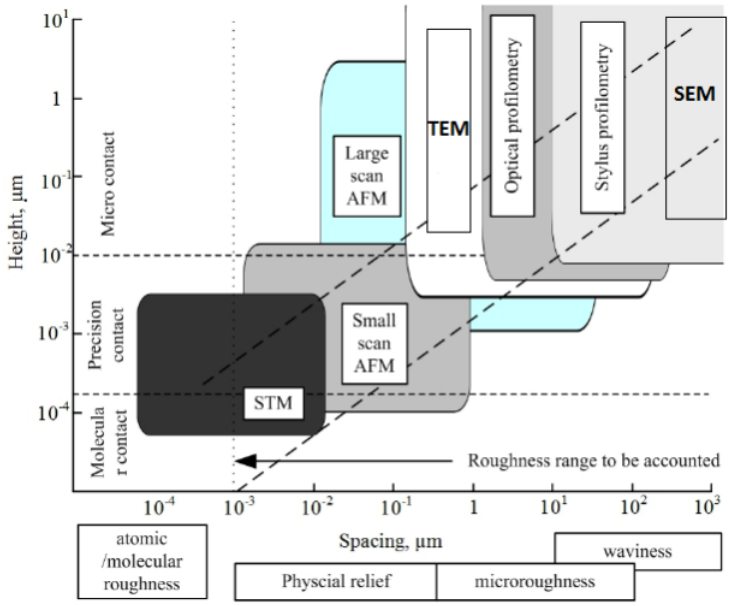

Figure 6: Diagram of the height and spacing parameters and ranges of vertical and lateral resolution for different methods of roughness measurement

If we dismiss instrumental difficulties, the formulation related to roughness structure with advanced measurement devices requires considering three fundamentals properties:

- Random roughness distribution
- Roughness multi-scale feature
- Non-homogeneity (which is showed as dependence between roughness parameters at its measurement scale)

In the group of the parameters which are contained in random distribution of roughness, are listed the height, slope and curvature at the top. Multi-scale character of roughness is due to the size of the roughness, which can vary from atomic scale up to the length of the sample. The mentioned properties are not independent.

It could be convenient to consider five main topographic levels related to the length scale: shape errors, ondulation, micro-roughness also named technologic roughness, sub-roughness or physical relief, and atomic-molecular roughness. However, in a practical way surfaces contain at least two different levels of roughness, ondulation plus roughness or roughness plus sub-roughness. Archard was the first person who made clear the great influence that this property makes in tribology; to be precise he proposed the multilevel model (Archard 1957).

Sayles and Thomas identified the non-homogeneity of the superficial topography as source of difficulties in the research (Sayles & Thomas 1978). From this point, Myshkin, Grigoriev et al. proposed a method to divide the topography measured by AFM into two levels: roughness and sub-roughness. This method achieve at least one of the two conditions to get homogeneity, which is to obtain a null average value. To delete the great wavelength component from roughness measure they used an image filtering process of repeat average. The roughness parameters in a scale lower than a micro-meter, sub-roughness, are determined with images of 10 μm x 10 μm and a resolution of 128 x 128 points.

In dry friction problems, the mathematical description of the rough surface allows the inclusion of the main features founded on the measurements. This inclusion provides the possibility to use models based on numeric simulation which goes from the simplest one, deterministic, which describe the rough surface like a regular groups of simple geometric bodies, up to complex models, based on the probability theories and fractal geometry (Patir 1978; Hu & Tonder 1992).

In this way, the real contact is a combination of punctual contacts, in which the total area is named physical contact area or real contact area. Latter is formed by roughs which contact in a nano-metric scale, what is called sub-roughness. The surface area of the physical contact is smaller than the support surface, apparent contact area, in one or two magnitude levels. Latter information is certified by the relation between the physical contact area, which supports a load, and the electric current that flows through that contact. An investigation work well-defined treats the analysis of the effect of this roughness in the friction coefficients. The classical friction coefficient could result useful in this cases, conveniently modify to accomplish the behaviour founded experimentally. For this reason, this coefficient can only be used for selected materials and an enclosed load values. Despite of the mentioned limitations, the latter models based in friction coefficient are useful to study devices submitted to certain loads and dragging velocities, because it shows interesting transitions between steady, periodic and chaotic dragging velocities. The knowledge about the values of the parameters which determine each of these states is so important for a correct design and operation of these devices.

Latter models have been numerically simulated by different methods such as finite differences or molecular dynamics (Hlscher, Schwarz et al. 1996).

1.2.2 Hysteresis effects on dry friction

Models of dry friction have been researched since Coulomb hypothesis (Coulomb 1785). In the first place, it results precise to emphasize on the existence of a wide variety of models which effectiveness depends on the, already modelled, problem's features. To be precise, if the dynamic of a system in which dragging velocity remains in a steady state is considered, there is no reason to use a com-

plex model; even the simplest one, described only by Colulomb's law, would be enough. For more complex dynamic behaviour systems with chaotic responses (Den Hartog 1931; Tolstoi 1967; Shaw 1986; Popp & Stelter 1990; Wojewoda, Barron et al. 1992; Feeny & Moon 1994; Wiercigroch 1994; Oestreich 1998; Bogacz & Ryczek 2003), the chosen model must consider transition between static and dynamic friction, being necessary furthermore the behaviour definition of the system while relative velocity is null. This model have to incorporate:

- The hysteresis, which explains pre-dragging or stick state
- The friction retard or irreversibility of the friction force
- Other characteristic phenomenon of friction like Stribeck effect or static variable friction force

However, unify all the effects related to friction in a single model is not an easy purpose. In fact, it's very difficult to define a mechanism that domains the transition between stick state and dragging or slip state. In the two last decades various friction models have been researched, which include mentioned properties (Armstrong-Hlouvry 1991; Powell & Wiercigroch 1992; Armstrong-Hlouvry, Dupont et al. 1994; de Wit, Olsson et al. 1995; Mc Millan 1997; Liang & Feeny 1998; Al-Bender, Lampaert et al. 2004). These models are so sophisticated to apply to mechanical devices because is difficult to find the proper values of the parameters which belong to the phenomenon.

If friction force is defined as the reaction in the tangent direction to both contact surfaces at the contact point, its value would depends on the normal force between both surfaces and various factors named above such as: physical properties of the materials that compound the contact surfaces, shape and topology, relative velocity and the motion of the bodies being in contact. In 1785, Coulomb (Coulomb 1785), in his first description didn't consider the relative velocity effect. Since the beginning of the 20^{th} century, the issues have been showing non-linear dependence between friction force and relative velocity (Stribeck 1902 (1); Stribeck 1902 (2); Rabinowicz 1951). These issues were done frequently in steady conditions. In fact, Stribeck's work (Stribeck 1902 (1); Stribeck 1902 (2)) shows the non-linear transition from the stick to the slip state. Stribeck effect (Stribeck 1902 (1); Stribeck 1902 (2)) consists in the decrease of the friction force for almost null values of relative velocity, Figure 7. Rabinowicz (Rabinowicz 1951) focused in the measure of the maximum value of friction force which appears on stick-slip transition, the force required to break the stick state, which allows system to begin motion. Studies related to these values have shown that its magnitude depends on the increase speed of friction force during stick state (Johannes, Green et al. 1973). So, while the increase of friction force becomes more rapid, minor

is the maximum value of the force. Maximum values of friction force are also related with the amount of time spent at null relative velocity, Figure 8.

The next group of features about friction to take in account is related to hysteresis effects. One of them can appear during stick phase and transition between stick-slip phases, it is produced by behaviour very similar to a spring. The microscopic motion phenomenon, stick phase, is related to tangential contact stiffness (Courtney-Pratt & Eisner 1956; Harnoy, Friedland et al. 1994; Liang & Feeny 1998). Motion on stick phase is represented by a weak width of hysteresis cycle, which appears around null values of relative velocity, Figure 9.

Other hysteresis effect appears when the displacement of the body oscillates during slip phase. These relative displacements are greater than stick phase displacements. This phenomenon was documented for the first time for a fluctuant relative velocity by Hess & Soom (Hess & Soom 1990), Figure 10. The surface of hysteresis increases the more rapid are the relative velocity variations (Olsson, Astrom et al. 1998). Friction force is greater when relative speed increases than when it decreases. So, dynamic behaviour can be explained considering'friction memory' caused by permanence at concrete values of friction force. Alternative fluctuations of relative velocity are associated with hysteresis also, Figure 11. Some theoretical and experimental studies have stated the existence of different slopes related to friction force during acceleration and deceleration (Den Hartog 1931; Bell & Burdekin 1970). This feature is known as friction force irreversibility (Powell & Wiercigroch 1992; Wiercigroch 1993; Wiercigroch, Sin et al. 1999).

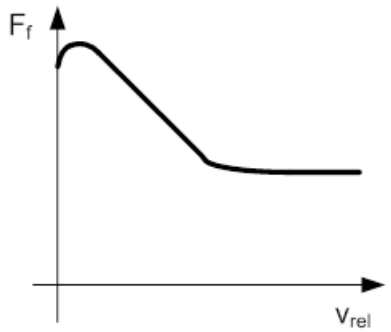

Figure 7: Friction force versus relative velocity

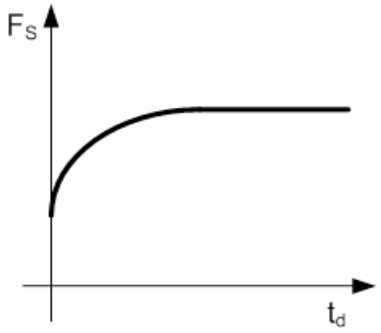

Figure 8: Maximum friction force versus permanence time at null relative velocity

1.2.3 Friction force formulation

Static models of friction don't include hysteresis phenomenon, represented by irreversibility or a delay on friction. From a general point of view, these models represent the direct dependence between friction force and relative velocity. Dynamics friction models, which include hysteresis processes, introduce states parameters which characterize friction and a differential equation related to the temporal evolution of this parameters (Wojewoda, Stefanski et al. 2008).

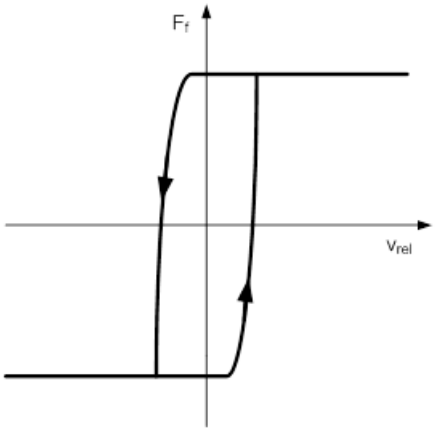

Figure 9: Hysteresis during stick

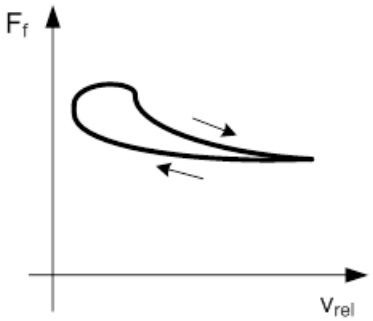

Figure 10: Hysteresis during slip-Fluctuant force

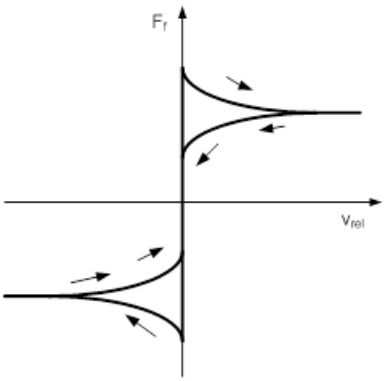

Figure 11: Hysteresis during slip-Alternant force

A point of view related to engineering, due to Coulomb's laws, simplify friction force, Ff, representing it as a constant value of opposite sign to relative velocity, v_{rel}, of the bodies being in contact; this is:

$$F_f = -N \cdot \mu_c \cdot sgn(v_{rel}) \tag{2}$$

where N is the normal load and μ_c the Coulomb's friction coefficient, Figure 12. This classic model is the simplest one and doesn't explain in practice the dynamic behaviour being observed in mechanical systems related to friction. To be precise, mathematical model of auto-excited vibrations, induced by dry friction, requires a non-null slope of friction force for begin this kind of oscillations (Babakiov 1968). Other disadvantage of Coluomb's model about friction force is that the physical interpretation of its response in the null relative velocity zone is missing. This fact justify the need of improve this model, stating a null value when change of sign is produced while relative velocity is zero.

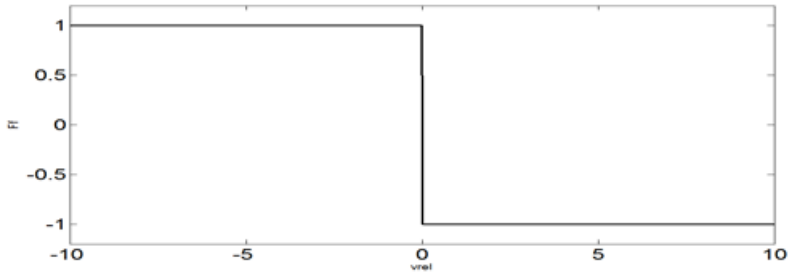

Figure 12: Representative graphic of Coulomb's law, friction force versus relative velocity

An improved version of the latter model includes the distinction between stick and slip phases:

$$\begin{cases} |F_f| \leq \mu_S \cdot F_N = F_S; \text{ if } v_{rel}=0 \\ F_f = -sgn(v_{rel}) \cdot \mu \cdot F_N; \text{ if } v_{rel} \neq 0 \end{cases} \tag{3}$$

where μ_S is the static friction coefficient, F_N the normal force, μ the dynamic friction coefficient and F_f the friction force. The dynamic friction force can be defined in function of relative velocity using the next expression:

$$\mu = \frac{\mu_S}{1 + \delta \cdot |v_{rel}|} \tag{4}$$

The δ parameter of the equation (4) allows considering the Stribeck's feature to the friction force expression, Figure 13.

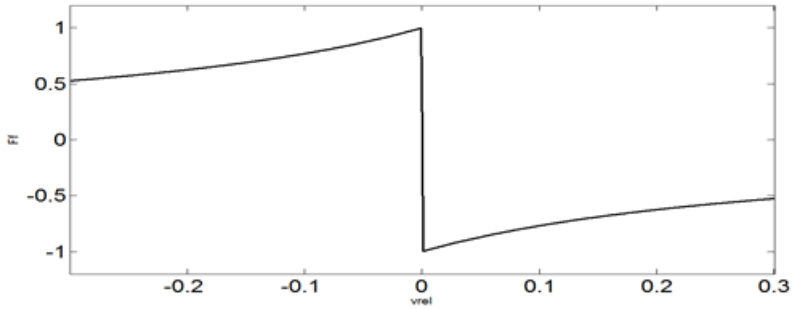

Figure 13: Stribeck's feature added to friction force (δ=3)

In Figure 13 abrupt change of friction force can be observed when a change in relative velocity is produced. A way to smooth this transition is to substitute the'sgn(z)' function by'$(\frac{2}{\pi})$arctan($\varepsilon \cdot z$)' (Andrianov, Awrejcewicz et al. 2005), where'ε' represents accuracy parameter, which controls the transition smoothness and'z' represents the argument of the function. Figure 14 shows this function for different values of'ε'.

Despite of this change, discontinuity can't be neglected, due to this, is difficult to ensure convergence in numeric solutions. The last change is based on introduce a null value of friction force at the moment in which relative velocity also changes its sign.

Other models with non-linear features of friction, can be written using the next expression:

$$F_f = -N \cdot \mu_C \cdot \left(1 + \frac{c}{\mu_C} \cdot g(v_{rel})\right) \cdot sgn(v_{rel}) \tag{5}$$

where μ_S is the static friction coefficient and g(v_{rel}) a non-linear function which describes Stribeck characteristic curve.

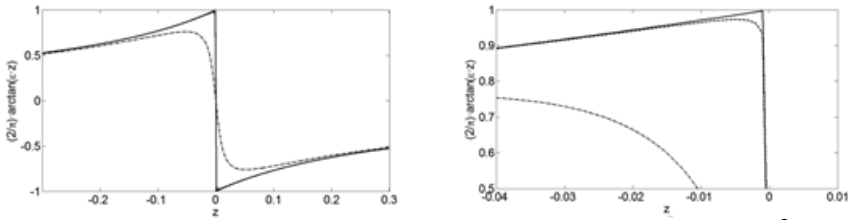

Figure 14: Approximation of'sgn(z)' function. For'ε'=1E^2 (traces and dots line),'ε'=1E^4 (traces line), y'ε'=1E^6 (continuous). Entire representation (left) and zoom out of the upper left corner (right)

Most usual formulations about the relation between relative velocity and friction force are the next ones:

- Exponential (Tustin 1947):

$$exp(-\frac{|v_{rel}|}{\nu_S}) \tag{6}$$

- Generalized exponential (Bo and Pavelescu 1982):

$$exp(-\alpha \cdot |v_{rel}|^{\delta}) \tag{7}$$

- From Gauss (Armstrong-Hlouvry 1991):

$$exp\left(-(\frac{v_{rel}}{\nu_S})^2\right) \tag{8}$$

- From Laurentz (Hess & Soom 1990):

$$\frac{1}{1 + (\frac{v_{rel}}{\nu_S})^2} \tag{9}$$

- From Popp-Stelter (Popp & Stelter 1990):

$$\frac{1}{1+\eta_1 \cdot |v_{rel}|} + \frac{\eta_2 \cdot v_{rel}^2}{\mu_S - \mu_C} \tag{10}$$

where α, δ, η_1 and η_2 are constants values and v_S is Stribeck's velocity, which is the limit of the relative velocity between stick and slip phases.

Models which include acceleration terms also include information about the change related to the retard time associated with hysteresis processes. This effect is called memory of friction.

Latter concept, associated with hysteresis effects in addition to elasticity contact, requires models of friction even more sophisticated. Powell, Wiercigroch et al. (Powell & Wiercigroch 1992; Wiercigroch, Sin et al. 1999) proposed a simple approach about the hysteresis behaviour during slip phase, based on the irreversibility associated with friction processes. This symmetric cases of irreversible friction, Figures 10 and 11, can be softly changed in equation 5, using a non-linear function which includes the sign of relative acceleration v_{rel}:

$$g(v_{rel}) = exp(-\alpha \cdot |v_{rel}|) \cdot sgn(v_{rel} \cdot tv_{rel}) \tag{11}$$

Other standpoint is related to seven parameters model, which can be described as a static model of hysteresis behaviour (Armstrong-Hlouvry 1991; Armstrong-Hlouvry, Dupont et al. 1994). Latter is even more complex than which includes friction irreversibility, due to both models which include: one related to stick phase and other associated with slip phase.

When system is operating in stick phase, friction can be described by lineal-spring model:

$$F_f(x) = k_S \cdot x \tag{12}$$

where k_S represents contact stiffness associated with the pre-displacement in slip phase. During slip phase, friction is modeled by means of Coulomb's force, F_C, a viscous damping, d_v, Stribeck's effect and memory of friction:

$$F_f(v_{rel},t) = [F_C + d_v \cdot v_{rel} + F_S(\gamma,t_d) \cdot \frac{1}{1+\left(\frac{v_{rel}\cdot(t-\tau)}{v_S}\right)^2} \cdot sgn(v_{rel})] \tag{13}$$

where $F_S(\gamma,t_d)$ denotes the value of static friction, which depends on a empiric parameter γ and remaining time t_d, the delay time τ considers hysteresis effect on memory of friction.

Numeric implementation of these static models shows the problem related to the change between equations 12 and 13 during stick-slip transitions.

From a classical standpoint, static models use static relations between friction force and velocity, and also with acceleration. Hunt, Torbe et al. (Hunt, Torbe et al. 1965) proposed this relation for the first time. Other example from a similar approach was purposed by McMillan (McMillan 1997) and Stefanski, Wojewoda et al. (Stefanski, Wojewoda et al. 2003). Latter model was based on friction irreversibility, equations 5 and 11, using the function:

$$g(v_{rel}) = exp\left(-\frac{a_1 \cdot |v_{rel}|}{|\dot{v}_{rel}| + a_2}\right) \cdot sgn(v_{rel} \cdot \dot{v}_{rel}) \tag{14}$$

where a_1 and a_2 are constant values. The first dynamic model, purposed by Dahl (Dahl 1968), uses tension-deformation of Ramberg and Osgood (Ramberg & Osgood 1943):

$$\frac{dF_f}{dx} = k_S \cdot \left(1 - \frac{F_f}{F_C} \cdot sgn(v_{rel})\right)^{\alpha} \tag{15}$$

where k_S, is the stiffness coefficient and α determines the shape of tension-deformation curve. Guessing F_f=k_S·z and α=1, equation 15 can be rewritten as:

$$k_S \cdot \frac{dz}{dx} = k_S \cdot \left(1 - \frac{k_S \cdot z}{F_C} \cdot sgn(v_{rel})\right) \tag{16}$$

Multiplying both terms of latter equation by $\frac{dx}{dt}$, v_{rel}, and simplifying, it results:

$$\frac{dz}{dt} = v_{rel} - \frac{k_S \cdot z}{F_C} \cdot v_{rel} \cdot sgn(v_{rel}) = v_{rel} - \frac{k_S \cdot |v_{rel}|}{F_C} \cdot z \tag{17}$$

where z means the state variable. Equation 15 is a dynamical generalization of Coulomb's classic friction. However, this standpoint doesn't include neither Stribeck's effect nor static friction.

Other dynamic model, concretely the one proposed by Bliman and Sorine, called LuGre model, save relation with roughness behaviour during friction leaded by the equations:

$$\begin{cases} \frac{dz}{dt} = v_{rel} - \frac{k_S \cdot |v_{rel}|}{g(v_{rel})} \cdot z \\ F_f = k_S \cdot z + c_S \cdot \frac{dz}{dt} + c \cdot v_{rel} \end{cases} \tag{18}$$

where z denotes, in this case, the roughness average deviation; coefficients k, and c, define the stiffness and damping of roughness, respectively; $c \cdot v_{rel}$ is viscous friction; and, $g(v_{rel})$ is a function which models Stribeck's effect following equation 8.

An advantage of LuGre model is its good dynamic behaviour, which make possible simulate stick-slip transitions, fluctuant static friction forces, memories of friction with hysteresis effects, and Stribeck's curve. Al-Bender, Lampaert et

al. (Al-Bender, Lampaert et al. 2004) model can be classified as an update of LuGre model.

Hinrichs, Oestreich et al. introduced an stochastic component to simulate the influence of some random factors, variations of normal force, and the non-homogeneity of roughs (Hinrichs, Oestreich et al. 1998).

Before this revision, it can be affirmed that the most part of stochastic models, equations 2, 3, 6 and 11, used to be only the first approximation. Concretely, latter doesn't describe with accuracy stick-slip transitions. However, its advantage is embedded in its simplicity and applicability in numeric simulations. Dynamics models, equations 15-18, and some advanced stochastic models, equations 12 and 13, allow to model with more accuracy the most part of observed phenomenon, even though they are generally more complex and harder to implement numerically.

1.2.4 Dynamic systems

A criterion to classify dynamic systems is the kind of temporal response. From this standpoint, future behaviour of random systems can only be assessed from a statistical point of view; latter is not the case of periodic systems, which came out periodically to the same position. Chaotic systems are supposed to be classified in an intermediate way, although they are as much sensitive to initial conditions as periodic systems (Nicholls & Tagarev 1994).

Figure 15 shows the nonlinear equation x_{i+1}=4·x_i-4·x_i^2, for two initial values of x_1=0.7 and x_1=0.70001 (Nicholls & Tagarev 1994). At the beginning both results don't seem different, but after some time the response becomes totally different. Predictions between points which are close to each other, results right because the small variation hasn't grown enough to take its effect into account. Chaos theory provides patrons of systems behaviour, when this is possible, when not it defines conditions to distinguish if the system behaviour would be unpredictable.

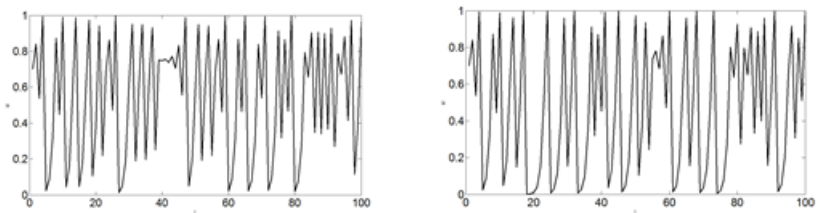

Figure 15: Differences between behaviours of a chaotic system for two initial values separated by 0.00001. x_1=0.7 (left) and x_1=0.70001 (right)

One of the classifications of these systems is associated to functional dependence. This way, dynamic systems are classified in: autonomous and non-

autonomous (Parker & Chua 1987). An autonomous system of'n' order is defined by state equation:

$$\dot{x} = f(x); x(t_0) = x_0 \tag{19}$$

As $\frac{dx}{dt}$ doesn't depend on time, t_0=0 can be fixed. A non-autonomous system of'n' order is defined by state equation:

$$\dot{x} = f(x,t); x(t_0) = x_0 \tag{20}$$

Other interesting concept is trajectory, $\phi_{t(x_0)}$, which is defined as solution of equation 19 for a single value of x_0.

The behaviour of a system may have various kinds of solution: equilibrium points, periodic solutions, almost-periodic solutions and chaos. This classification is related with the representation of the solutions on phase's space. From this standpoint, parallelism between features of an autonomous system and a vector field can be highlighted (Banerjee 2005):

- The vector embedded in any point of a state space is unique
- The field's lines can't intersect between them, except in points in which $\frac{dx}{dt}$ gets null, equilibrium points
- Right member of each equation of the state's equation system is derivable in its entire domain

If a linear approximation of the equation system in the equilibrium points is done, auto-vectors obtained define the beginning of the field's lines and the state's evolution.

When state's equation systems are assessed out of the equilibrium point, linear approximations begins to make no sense as we get far of latter point. As a consequence, lines begins with an auto-vector in the proximities of an equilibrium point doesn't remain straight, Figure 16. These curved lines are called invariant varieties, which have the property of if an initial condition is embedded in the variety, the future values of the state's variables remains in this variety. Stable and unstable auto-vectors in the equilibrium point are tangent to the varieties in that point (Banerjee 2005).

There is a fundamental difference between the periodic behaviour of linear systems with imaginary auto-values and periodical trajectories of non-linear systems, limit cycles. In the case of a non-linear system with limit cycle, trajectories begin from different initial conditions converging to the same periodic behaviour, limit cycle. Latter can be called also periodic attractor.

In non-linear dynamic systems with various periods it may occur that these would be commensurable, a rational number, in this case trajectory is periodic. If

these periods are non-commensurable the state never repeats and trajectory is an almost-periodic one.

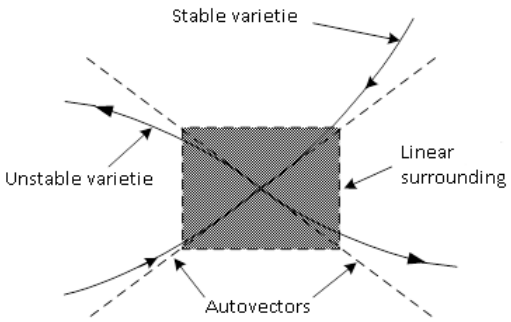

Figure 16: Stable and unstable varieties in a saddle point

In third order systems or upper, trajectories remains confined within a finite element in a phases space, but these are never repeated. This situation is denominated chaos; resultant attractor is denominated strange attractor. Basic difference between almost-periodic and chaotic systems is the sensitiveness of these to initial conditions.

Space of phase, already mentioned, provides a deeper interpretation of chaotic behaviour. Even more chaotic is the system, then more are the number of trajectories and more disordered seems the attractor within the space of phases. In these cases, it's possible to simplify the representation of the attractor using a bi-dimensional section, Poincare's map.

Before defining Poincare's map, it results necessary to consider the relation between autonomous and non-autonomous systems. A non-autonomous system of order n and period of value T, can be transformed in an autonomous system of n+1 dimension, habitually a cylindrical $\mathbb{R}^n \times S$ state space. This space may be dissected by a n-dimensional hyper-plane:

$$\Sigma=\{(x,\theta) \in \mathbb{R}^n \times S \ / \ \theta=\theta_0\}$$

So, for the case in which n=1, each T seconds the trajectory intersects Σ, as can be appreciated in figure 17. Intersections P(x), Poincare's application, constitute Poincare's map. From other standpoint, for an autonomous system of n order and limit cycle Γ, with minimum period of value T, can behave in a similar way. Considering an hyper-plane Σ of n-1 dimension, trajectory intersects the latter each T seconds. Intersection points, x*, constitute Poincare's map. In figure 18 can be appreciated an autonomous system of third order and its Poincare's section.

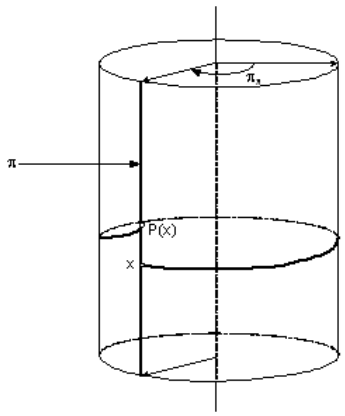

Figure 17: Poincare's map of a non-autonomous system of first order (Parker & Chua 1987)

There is a unique reciprocation between the behaviour of the system and P, intersection of trajectory with Σ, this is, Poincare's map. Fixed points, periodic orbits, limit cycles and attractors are kind of limit sets.

1.2.5 Stability of limit sets: characteristics multipliers

One of the main goals of the dynamic systems studies, consists in determine the stability of any kind of steady behaviour, including almost-periodic and chaotic systems. To develop suitable tools in this study is necessary to carry out a more detailed analysis of the equations.

From the equation of an autonomous system of order n, solution near of the equilibrium point, x_{eq}, is obtained through the next linearization:

$$\delta\dot{x} = Df(x_{eq}) \cdot \delta x \tag{21}$$

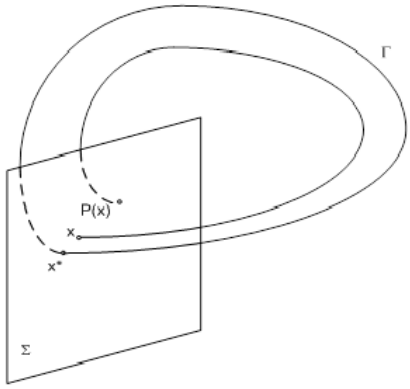

Figure 18: Poincare's map of a non-autonomous system of third order (Parker & Chua 1987)

Obtained trajectory from the initial condition of x_{eq}+δx_0 is:

$$\phi_t(x_{eq}+\delta x_0) = x_{eq}+\delta x(t) = x_{eq}+c_1\cdot\eta_1\cdot e^{\lambda_1\cdot t}+\cdots+c_n\cdot\eta_n\cdot e^{\lambda_n\cdot t} \tag{22}$$

Where λ_i and η_i are auto-values and auto-vectors of Df(x_{eq}) respectively, and c_i is a scalar constant obtained from initial condition. Real part of λ_i means the expansion ratio of the trajectory when it is greater than zero, or contraction ratio when it is lower than zero, in the nearness of the equilibrium point, x_{eq}, in the direction of η_i. If real part of λ_i is lower than zero for any value of'i', any perturbation small enough tends to zero, and the system is asymptotically stable. If real part of λ_i is greater than zero for some value of'i', x_{eq} isn't stable. In the last case there are two possibilities: unstable, if real part of λ_i is greater than zero for any value of'i', and non-stable if real part of λ_i is lower than zero for some value of'i', the stability can't be determined only by auto-values. Equilibrium points in which all auto-values have null real part are denominated hyperbolic. These points have the feature of other near points, equilibrium point plus small perturbations, have the same stability. This property is called structural stability. For periodic systems, stability of the solution is determined by the stability of the unique point that composes the Poincare's map, fixed point. Similar to the facts mentioned about the equilibrium point, the stability of a point from the Poincare's map, x*, is determined by the linearization of the Poincare's application, P(x), in x*:

$$\delta x_{k+1} = DP(x^*)\cdot\delta x_k \tag{23}$$

Poincare's application related to a trajectory with initial value of x_0+δx_0 is:

$$x_k = x^*+\delta x_k = x^*+c_1\cdot\eta_1\cdot m_1^k+\cdots+c_p\cdot\eta_p\cdot m_p^k \tag{24}$$

where m_i^k and η_i are auto-values and auto-vectors of DP(x*) respectively, p is the dimension of DP(x*) and c_i is a scalar constant obtained from initial condition. The value of parameter p is n, for non-autonomous systems, and n-1 for autonomous systems.

Auto-values are the characteristic multipliers of the fixed point, also denominated Floquet's multipliers. These determine the contraction ratio if $|m_i|<1$, or the expansin ratio if $|m_i|>1$, near of x* in the direction of η_i for each iteration of Poincare's map.

Similarly to already mentioned facts related to the equilibrium point of a system, if all m_i, are inside a circle of unitary radius, the periodic solution is asymptotically stable. If all $|m_i|$ are greater than one, the solution is periodic and unstable. If one of the characteristic multipliers is on the circumference of unitary radius, the stability of the solution can be determined only through these. The periodic solutions with all the characteristic multipliers embedded on the unitary radius circumference are called hyperbolic solutions, and they are structurally stable.

Autonomous periodic systems doesn't have explicit expressions about P, because of this it results impossible to obtain DP(x*). However, autonomous systems at least have one auto-value equal to 1, the stability depends on the limit sets of the n-1 remaining auto-values.

If solution of equation 19 in x_0 as $\phi_t(x_0)$, auto-values can be assessed through differential equation obtained deriving the equation respect x:

$$D_{x_0}\dot{\phi}_t(x_0) = D_x f(\phi_t(x_0)) \cdot D_{x_0}\phi_t(x_0) \tag{25}$$

where $D_{x_0}\phi_t(x_0)$=I.

If $D_{x_0}\dot{\phi}_t$ is defined as $\dot{\Phi}_t$ the equation 25 turns on:

$$\dot{\Phi}_t(x_0) = D_x f(\phi_t(x_0)) \cdot \Phi_t(x_0) \tag{26}$$

In the case of non-autonomous periodic systems, equation 20, which solution in (x_0,t_0) is $\phi_t(x_0,t_0)$, can be written as:

$$\dot{\phi}_t(x_0,t_0) = f(\phi_t(x_0,t_0),t) \tag{27}$$

And the derivative respect to x_0:

$$D_{x_0}\dot{\phi}_t(x_0,t_0) = D_x f(\phi_t(x_0,t_0),t) \cdot D_{x_0}\phi_t(x_0,t_0) \tag{28}$$

where $D_{x_0}\phi_{t_0}(x_0,t_0)$=I.

Using a similar notation of the equations 26 and 28 can be rewritten as:

$$\dot{\Phi}_t(x_0,t_0) = D_x f(\phi_t(x_0,t_0),t) \cdot \phi_t(x_0,t_0) \tag{29}$$

Conclusions about equation 29 may be:

- $D_x f(\phi_t(x_0,t_0),t)$ is a matrix which varies with time, so, differential equations system is linear respect to time of n^2 order
- $\Phi_t(x_0,t_0)$ is the state's transition matrix of the system:

  $$\delta\dot{x} = D_x f(\phi_t(x_0,t_0),t) \cdot \delta x \tag{30}$$

  where $\delta x(t_0)=\delta x_0$ and $\delta x(t)=\Phi_t(x_0,t_0)\cdot\delta x_0$ is the response of the system to a small perturbation, δx_0. It's trivial that $\Phi_t(x_0,t_0)$ controls the trajectory of the response to a small variation of initial value
- Differential equation is the linearization of $\frac{dx}{dt}$ of trajectory $\phi_t(x_0,t_0)$

If Poincare's application is defined as $\phi_T(x_0,t_0)$, its auto-values are given by:

$$D_{x_0}\phi_T(x^*,t_0) = \Phi_T(x^*,t_0) \tag{31}$$

Auto-values are the characteristic multipliers of a periodic solution of the system.

The simpliest way to link up characteristic multipliers and auto-values of $D_f(x_0)$ is to consider its equilibrium point, x_{eq}. This point can be treated as a limit cycle of period T.

$$\phi_t(x_{eq}) = x_{eq} \tag{32}$$

From equation 26 and considering x_0=x_{eq}, next expression is obtained:

$$\phi_t(x_{eq}) = e^{D_f(x_{eq})\cdot t} \tag{33}$$

This allows to link auto-values of $D_f(x_{eq})$, λ_i, with auto-values of $\Phi_t(x_0)$, which are the characteristic multipliers, through next function:

$$m_i = e^{\lambda_i \cdot T} \tag{34}$$

As $|m_i|<1$ when the real part of λ_i is lower than zero, m_i and λ_i provide the same information of the system's stability.

1.2.6 Stability of the limit sets: Lyapunov's exponents

Lyapunov's exponents are a generalization of auto-values of an equilibrium point and its characteristic multipliers. They're used to know the stability of any kind of steady behaviour, including almost-periodic systems and chaotic ones, if they are defined in terms of the differential equation solution:

$$\lambda_{Li} = \lim_{t\to\infty}\left(\frac{1}{t}\cdot ln(|m_i(t)|)\right) \tag{35}$$

If λ_i and η_i are the auto-value and auto-vector of $D_f(x_{eq})$ respectively, it results:

$$\lambda_{Li} = \lim_{t\to\infty}\left(\frac{1}{t}\cdot ln(|e^{\lambda_i\cdot t}|)\right) = \lim_{t\to\infty}\left(\frac{1}{t}\cdot Re[\lambda_i]\cdot t\right) = Re[\lambda_i] \tag{36}$$

In this specific case, the real part of the auto-values related to equilibrium point matches with Lyapunov's exponent. From this standpoint, if λ_{Li} is negative, it means the contraction ratio near of the equilibrium point. Otherwise if λ_{Li} is positive it means the expansion ratio. If x_0 belongs to an attraction region of x_{eq}, in other terms, $\phi_t(x_0)$ tends to x_{eq}, any finite non-steady phenomenon can be neglected and Lyapunov's exponents of x_0 and x_{eq} match with each other. In a

general way, every point situated in an attraction region have the same Lyapunov's exponent.

For cases related to limit cycles the relation between characteristic multipliers and Lyapunov's exponents is simpler:

$$\lambda_{Li} = \frac{1}{T} \cdot ln|m_i| \tag{37}$$

where λ_{Ln} takes zero value due to it is an auto-value of $\Phi_T(x^*)=1$, in the case of an autonomous system.

To continue, an analysis about if it is necessary to calculate all the Lyapunov's exponents is going to be carried out. If auto-values of a system with a single equilibrium point in the origin are entirely real, these match with the Lyapunov's exponent, equation 35. If Lyapunov's exponents are sorted from greatest to smallest, there are n linear subspaces $W_1 \subset \cdots \subset W_n$, with dimensions n, n-1,,1 respectively, they are defined as W_i=span$\{\eta_i, \eta_{i+1},, \eta_n\}$. So for W_n=span$\{\eta_n\}$, any initial condition $x_0 \in W_n$ evolves as:

$$x_0 \cdot e^{\lambda_{Ln} \cdot t} \tag{38}$$

For W_1=span$\{\eta_i, \eta_{i+1},, \eta_n\}=\mathbb{R}^n$, any $x_0 \in W_1 \setminus W_2 = \{x \in W_1 | x \notin W_2\}$ evolves as:

$$c_1 \cdot \eta_1 \cdot e^{\lambda_{L_1} \cdot t} + c_2 \cdot \eta_2 \cdot e^{\lambda_{L_2} \cdot t} + \cdots + c_n \cdot \eta_n \cdot e^{\lambda_{L_n} \cdot t} \tag{39}$$

As $\lambda_{L_1} > \lambda_{L_2} > \cdots > \lambda_{L_n}$ Lyapunov's exponents with subscript greater than one can be neglected after a while and initial condition x_0 evolves as:

$$x_0 \cdot e^{\lambda_{L_1} \cdot t} \tag{40}$$

Thus, this result shows that it's only interesting to consider the value of λ_1 in order to study the stability of the system.

Lyapunov's exponents can be used to classify steady behaviours, Table 1. For stable equilibrium points, Lyapunov's exponents are always negative. For limit cycles, $\lambda_{L_1}=0$ and the rest exponents are negative. For stable toroids, $\lambda_{L_1}=\lambda_{L_2}=0$ and the rest exponents are negative. For an attractor, contraction should exceed the expansion:

$$\sum_{i=1}^{n} \lambda_{L_i} < 0 \tag{41}$$

Table 1: Clasification of systems (Parker & Chua 1987)

Steady state	Flow	Poincare's map	Lyapunov's exponents	Dimension
Point		$0>\lambda_{L_1}\geq\lambda_{L_2}\geq\cdots\geq\lambda_{L_n}$	0	
Periodic	Curves near with each other	Point	$\lambda_{L_1}=0$ $0>\lambda_{L_2}\geq\cdots\geq\lambda_{L_n}$	1
Sub-armonic	Curves near with each other	Orbits near with each other	$\lambda_{L_1}=0$ $0>\lambda_{L_2}\geq\cdots\geq\lambda_{L_n}$	1
Double periodic	Toroid	Curves near with each other	$\lambda_{L_1}=\lambda_{L_2}=0$ $0>\lambda_{L_3}\geq\cdots\geq\lambda_{L_n}$	2
K-periodic	K-toroid	(K-1)-toroid	$\lambda_{L_1}=\cdots=\lambda_{L_k}=0$ $0>\lambda_{L_{k+1}}\geq\cdots\geq\lambda_{L_n}$	k
Chaotic	Almost-Cantor	Almost-Cantor	$\lambda_{L_1}>1$ $\sum_{i=i}^{n}\lambda_{L_i}<0$	Not integer

A strange attractor have at least one positive Lyapunov's exponent, although it can be defined only through Lyapunov's exponents. Some researchers have proposed to use transversal intersections of a varieties set in Poincare's map to define it (Parker & Chua 1987).

1.2.7 Assessing Lyapunov's exponents

The methods to assess Lyapunov's exponents which use temporal series are: The ones based on the Jacobian and the direct ones.

Jacobian based methods use jacobians matrixes of the model's equations to calculate Lyapunov's exponents through standard algorithms which have been developed in the cases in which equations of the dynamic systems are known. Usually linear approaches are used. Changes and improvements of basic algorithm include:

- The use of ranges near with each other instead of balls to reduce the noise influence
- The use of non-linear approaches of the trajectory through polynomials, radius basis networks or neuronal networks
- The use of projections on linear sub-spaces based on local coordinates of Broomhead-King

- The use of embedding dimension, d, to select the nearest points and a lower local dimension, d_L, to achieve the fit and the assessing of Lyapunov's exponents resulted of d_L

Two last variants try to avoid, commonly called, false Lyapunov's exponents, which appear when d dimension of rebuild state's space is greater than m dimension of the original state's space. This variants doesn't depend on the dynamic but of the approximation scheme, the noised related to these data and in particular cases the local curvature of the attractor. In principle, any set of values can be taken. The wide of the attractor along the directions related with all the Lyapunov's exponents and the comparison of the exponents obtained through the temporal series with the exponents calculated with the same temporal series with time inversion allows to identify false Lyapunov's exponents. Latter fact is due to that false exponents are related with directions where the attractor compress it section and due to that signs doesn't change when time is inverted. The last mentioned variant is used only with high accuracy data, which allow a right approach of negative Lyapunov's exponents.

Taking into account the importance of the reconstruction of phase's space in the assessment of Lyapunov's exponents, it's going to be explained with detail then. This phase's space is diffeomorphically equivalent to the original phase's space of the measured system. Based on the reconstructed spaces non-linear dynamic of the system can be analyzed.

Basically there are two methods to rebuild phase's spaces from scalar temporal series: coordinates with retard and derivative coordinates. As derivatives are noise-sensitive, they aren't used commonly with measure data. The measure of the scalar temporal series, s(t), is a function:

$$s(t) = h\left(\overrightarrow{x(t)}\right); h : M \to \mathbb{R} \tag{42}$$

M is a m-dimensional variety in which evolve of states, ϕ_t, are represented.

Delay, t_l, and embedding dimension, d, are obtained from:

$$\overrightarrow{y} = F(\overrightarrow{x}) = (s(t), s(t-t_l), \cdots, s(t-(d-1)\cdot t_l)); F : M \to \mathbb{R}^d \tag{43}$$

Figure 19 represents the rebuilt of phase's space from a scalar temporal series. Direct methods approach the divergent motion of rebuilt states. The most known and used method is the one introduced by Wolf, Swift et al. So, a reference trajectory $\{y^n\}$ and a near trajectory $\{z^n\}$ are considered, which begin from the nearest point of each curves, z^0 and y^0, Figure 20. After a non-steady period the difference vector u^k=z^{n+k}-y^{n+k} points to direction related to the greatest Lyapunov's exponents, λ_{L_1}. So $||u_k||$ grows, averagely, as $e^{\lambda_{L_1}\cdot t_s\cdot k}$ grows too untill the range wherein approach of $\{y^n\}$ remains linear. Trajectory $\{z^n\}$ has to be embedded by

other near trajectory which has to be closer to the reference trajectory, Figure 20, with the goal to preserve the direction related to the greatest Lyapunov's exponent. The criteria that are used for substitution threshold and other algorithm's features can be found on Wolf, Swift et al.

In principle, it is possible to use latter strategy to obtain the second greatest Lyapunov's exponent, but it turns some difficult. From other standpoint, in many cases it's enough to make clear the existence of at least a single positive Lyapunov's exponent. Wolf's algorithm is often used applied to experimental data because of his toughness.

Another direct method, which is even simpler, talking about the amount of free parameters, was proposed by Sato, Sano et al., & Kuths & Herzel. In the latter, very similar to Wolf's algorithm, the average exponential growing of the distance between close orbits is studied in a logarithmic scale, this time through the prediction:

$$p(k) = \frac{1}{N \cdot t_s} \cdot \sum_{i=1}^{n} log_2 \left(\frac{||y^{n+k} - y^{nn+k}||}{||y^n - y^{nn}||} \right) \tag{44}$$

where $\{y^{nn}\}$ is the closest trajectory to $\{y^n\}$.

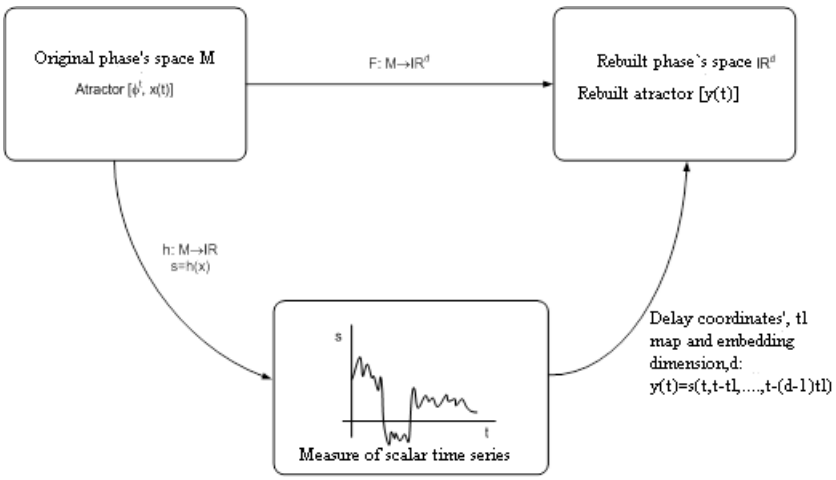

Figure 19: Reconstruction of the phase's space from a scalar temporal series

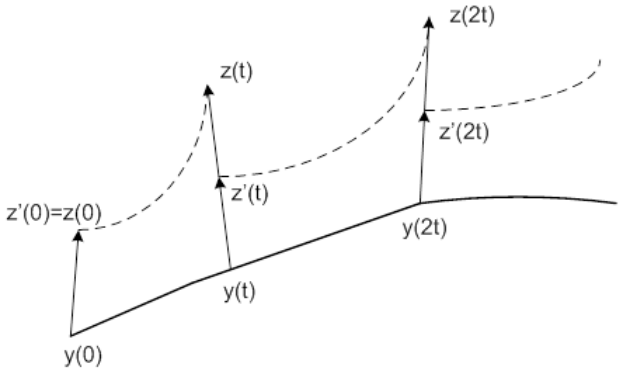

Figure 20: Trajectories selection scheme lead by Wolf procedure

The dependence of the prediction error p(k) on the time steps k can be divided in three phases. The first phase is characterized by a non-steady behaviour where closest orbit converge in the direction related to the greatest Lyapunov's exponent. During the second phase the distance grows due to $e^{\lambda_{L_1} \cdot t_s \cdot k}$ up to exceed the permissible range of the linear approach associated with the trajectory around the reference orbit $\{y^{n+k}\}$. Third phase starts where the distance grows slower than exponentially until it decreases again due to folds in the states' space. If second phase is large enough, a linear segment with slope of value λ_{L_1} appears in the graphic which faces p(k) before k, which is a temporal step. This doesn't only allow an approach of the greatest Lyapunov's exponents, λ_{L_1}, but also provides a direct verification of the distance's exponential growth, characteristic of deterministic chaos, unlike of the stochastic processes, with non-linear graphics.

An interesting feature of the function related to prediction error is the relation of its slope with the greatest Lyapunov's exponent. The application of the direct method obliges to use procedures of retarded selection and embedding dimension. Embedding theorems narrow the retard but they don't fix it. An underestimation of this time leads to rebuilt states which don't differ so much and which points are dispersed around a straight line. On the other hand, an overestimation leads to chaotic attractors which fold, with auto-iterations and a loss of correspondence between original states and rebuilt ones. Other aspect to take into account is the duration of the temporal series register, which is crucial to characterize the embedding dimension.

It has been proposed many methods to select the retard, the most commonly known consist in minimize the redundancy of the delay coordinates of the rebuilt states, equation 43, through auto-correlation linear functions or theoretical concepts of the information like mutual information. So, a good approach of the retard is obtained from the first minimal mutual information. From this value and using a method proposed by Cao, embedding dimension can be approached, which would be helpful to obtain the phase's space reconstruction.

1.3 Preliminary work

This work is related with one of the research lines of the research group Network Method that belongs to Technical University of Cartagena (UPCT). To be more precise this work deals with the analysis of dry friction in a Girling duo-servo brake mechanism.

The anti-lock breaking systems don't allow the wheels to be locked during an abrupt stop process, which improves the directional stability and make shorter the brake distance. A bi-dimensional and non-linear dynamic system with commutation control is one of the simplest anti-lock devices.

The non-linearity of the system shows the relation between the slip and the dynamic frictional coefficient.

Awrejcewicz uses a physical model of a brake system for one single wheel, which includes non-linear coefficients. Specifically, the'duo-servo' Girling brake was simplify using a two bodies and two degrees of freedom system.

In this way, the research group has studied, since several years, different frictional phenomenon (Marín, F., F. Alhama, et al. (2012). "Modelling of stick-slip behaviour with different hypotheses on friction forces."). Following these works, we had to analyze the running of a system equivalent to a Girling brake. The latter includes a block that slips and a crank articulated in its corner. The slipping block is connected to the frame using a linear-spring, which elastic constant is k_1. This block is also connected to the crank within two springs, the horizontal one has a elastic constant k_2 and vertical one has a elastic constant k_3.

The behaviour of the two last models is very sensitive to the function that defines the friction force, because of this the next part is going to deal the phenomenon in a much detailed way. Basically, it is necessary to consider roughness and hysteresis in the friction coefficient. Anyway, the discontinuity given in this phenomenon makes necessary to consider some facts on the friction formulation.

1.4 Only the main literatures

- Marín, F. (2013). Aplicación del método de redes a la solución de problemas de fricción seca: Superfices suaves a escala atómica y superficies a escala macroscópica. Doctoral Thesis

- Awrejcewicz, J. Y P. Olejnik (2003) (2). Numerical and experimental investigations of simple non-linear system modelling a girling duo-servo brake mechanism. DETC 2003 Chicago, ASME

- SignalExpress: Getting Started with SignalExpress August 2004 Edition. Part Number 37873A-01

- Banerjee, S. (2005). Dynamics For Engineers. John Wiley and Sons, Chichester, United Kingdom

2 Nature of the work

2.1 Introduction

The test of the frictional device equivalent to a Girling brake delivers important information about the behaviour of these systems. The understanding of these behaviours is valuable to the design of new devices. In present, this analysis is developed by numerical procedures, this means a non-realistic analysis of this processes. On the other hand, experimental method provides a closer analysis without assumptions with inadequate fundaments.

2.2 Aims of the tasks

The basic aim of the present work is the test of a frictional device that represents the behaviour of a Girling brake. In this study, we analyse the frictional processes by the displacement of a slipping block.

2.3 Useful effects

The results of this study allow a better understanding of devices that shows frictional phenomenon. In order to analyse this processes a virtual instrument, software which manages the signal from a probe and depicts a comprehensive graph with the useful information, has been implemented. One of the most difficult behaviours in frictional phenomenon, the stick-slip movement, is managed in a suitable way. Moreover, this study establishes the relationship between the operational velocity and the slipping displacement pattern.

2.4 Work in the future

There are many things to do.

- The establishment of the relation between numerical models and experimental tests, which aim for better characterization of frictional force model
- The development of more tests characterized with other parameters values
- The analysis of the hysteretical effects

3 Analyisis of literatures

- Marín, F. (2013). Aplicación del método de redes a la solución de problemas de fricción seca: Superfices suaves a escala atómica y superficies a escala macroscópica. Doctoral Thesis

  This work develops different frictional models, which of them is an equivalent device of the Griling brake. Moreover this analysis involves a test of this device and proposes new research tasks that are followed in this work.

- Archard, J. F. (1957). Elastic deformation and the laws of friction. Proceedings of the Royal Society of London. Series A. Mathematical and Physical Sciences 243(1233): 190-205.

  A classical reference that deals with the frictional basics.

- Awrejcewicz, J. Y P. Olejnik (2003). Numerical and experimental investigations of simple non-linear system modelling a girling duo-servo brake mechanism. DETC 2003 Chicago, ASME.

  This work proposes the experimental workbench of a equivalent device of a Girling brake. Even it deals with the signal analysis and important ideas about the management of the variables.

- Den Hartog, J. P. (1931). Forced vibrations with combined Coulomb and viscous friction. Transactions of the ASME APM 53(9): 107-115.

  A classical reference that deals with the frictional basics involving vibrational behaviours.

- Galvanetto, U. (2001). Some discontinuous bifurcations in a two-block stick-slip system. Journal of Sound and Vibration 248(4): 653-669.

  A classical reference that deals with the frictional basics involving vibrational behaviours. Even several comments about chaotic behaviour are provided.

- Girling (2013). http://www.girlingauto.com.

  A website with information about this kind of devices.

- Greenwood, J. A. y J. B. P. Williamson (1966). Contact of nominally flat surfaces. Proceedings of the Royal Society of London. Series A. Mathematical and Physical Sciences 295(1442): 300-319.

  A classical reference that deals with the frictional basics and frictional engineering.

- Hinrichs, N., M. Oestreich, et al. (1998). On the modelling of friction oscillators. Journal of Sound and Vibration 216(3): 435-459.

  A fine reference to understand frictional phenomenon with chaotic behaviours.

- Marín, F. et al. (2012). Modelling of stick-slip behaviour with different hypotheses on friction forces. International Journal of Engineering Science 60: 13-24.

  A current reference to understand frictional phenomenon with chaotic behaviours.

- Rabinowicz, E. (1951). "The nature of the static and kinetic coefficients of friction." Journal of Applied Physics 22(11): 1373-1379.

  A classical reference that deals with the frictional basics.

- Stribeck, R. (1902). Fundamental characteristics of the friction bearing and the roller bearing. Zeitschrift des Vereines Deutscher Ingenieure 46: 1341-1348.

  A classical reference that deals with the frictional basics.

- Banerjee, S. (2005). Dynamics For Engineers. John Wiley and Sons, Chichester, Reino Unido.

  A reference that deals with chaotic topics.

- Cao, L. Y. (1997). Practical method for determining the minimum embedding dimension of a scalar time series. Physica D 110(1-2): 43-50.

  A reference that deals with chaotic topics.

- Geist, K., U. Parlitz, et al. (1990). Comparison of different methods for computing Lyapunov exponents. Progress of Theoretical Physics 83(5): 875-893.

  A reference that deals with software relative to chaotic behaviours analysis.

- Parker, T. S. y L. O. Chua (1987). Chaos - A tutorial for engineers. Proceedings of the IEEE 75(8): 982-1008.

  A reference that deals with chaotic topics.

- Sato, S., M. Sano, et al. (1987). Practical methods of measuring the generalized dimension and the largest Lyapunov exponent in high dimensional chaotic systems. Progress of Theoretical Physics 77(1): 1-5.

  A reference that deals with chaotic topics.

- Wolf, A., J. B. Swift, et al. (1985). ”Determining Lyapunov exponents from a time-series.” Physica D 16(3): 285-317.

  A reference that deals with chaotic topics.

- SignalExpress: Getting Started with SignalExpress August 2004 Edition. Part Number 37873A-01.

  It’s the reference used to develop the software in the management experimental data.

4 Methods

4.1 Introduction

The subject of this project is the characterization of a Girling duo-servo brake mechanism. To realize the analysis of the latter mechanism it had been used the software Signal Express and Matlab, to manage the experimental data. The software Signal Express provides the tool to collect the data and Matlab allows representing it properly; even to operate with the data to obtain graphs which show more relevant information about the phenomenon being studied.

The results provided by software Matlab are useful to understand better the processes of the girling duo-servo brake mechanism at different operation velocities.

4.2 Mechanical system's design

As has been said in the section 2.2, in this section a device, Figure 21, that simplify the Girling duo-servo brake mechanism is studied. This device produces the stick-slip phenomenon and consists of a set of springs and a block. After several preliminary tests, springs of 0.14 and 0.34 N/mm has been selected in order to get displacements inside of the measure range of the commercial probes. For the same reason a block's mass of 195.3 g has been chosen. Moreover the springs are guided by sleeves to avoid them to bend on its longitudinal axis.

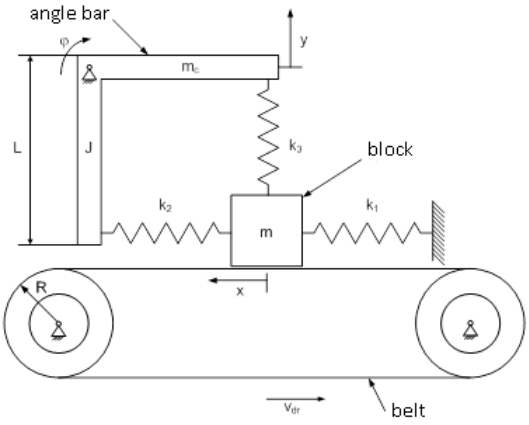

Figure 21: Simplification of girling duo-servo brake mechanism

Figure 22 shows the fastenings of the springs in the crank and block.

Figure 22: Fastenings of the springs

Enclosure A includes the drawings used in the manufacture of this device. This work has been developed in the Taller Mecnico de Apoyo a la Investigacin belonged to the Servicio de Apoyo a la Investigacin Tecnolgica.

4.3 Measures system's design

After several preliminary tests with different probes, a laser difractometer and an infrared optoelectronic device, with negative results, it has been chosen a laser distance sensor. The measure system consist of the above sensor, Omron Z4M-S40, a signal amplifier, Omron Z4M-W40, an acquisition card, NI-9205, and a computer with an Intel Core 2 Quad processor. The signal is processed by Signal Express software, 3rd version, belonged to LabView software. In order to show the results in a more proper way, Matlab software has been used to depict the measures.

The characteristics of the laser distance sensor are:

- Sensing distance: 40 mm
- Measurement range: 10 mm
- Resolution (at response time): 1.5 m (60 ms), 10 m (2 ms), and 40 m (0.15 ms)
- Sensitivity: 0.4 V/mm

The characteristics of the acquisition card are:

- Sampling rate: 250 kS/s

- Number of channels: 32 single-ended or 16 differential analog input channels, 1 digital input channel, and 1 digital output channel
- ADC resolution: 16 bits
- Nominal input ranges: 10 V, 5 V, 1 V, 0.2 V

The software Signal Express has been set up to depict a first view of the signal. After this verification the signal has been recorded in a text file to be managed with a routine written in Matlab. The Figure 23 shows a screenshot of the Signal Express with the set up.

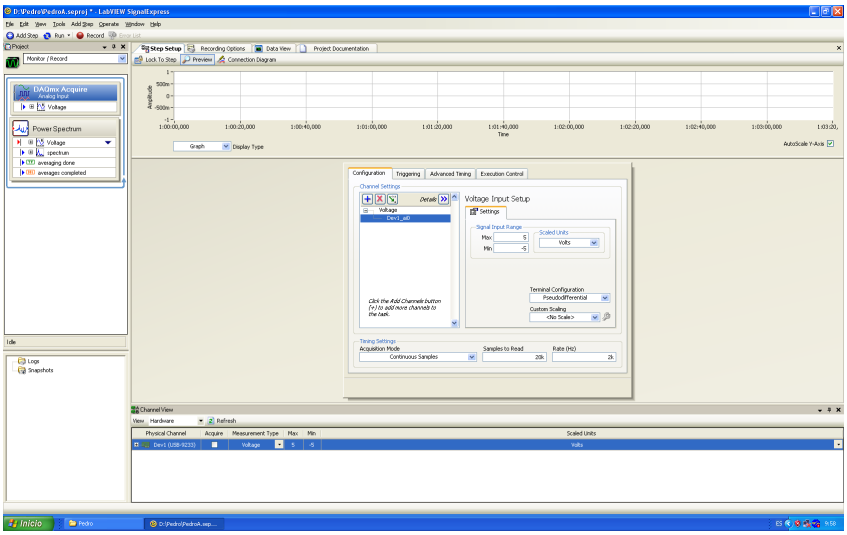

Figure 23: Screenshot of the measures' set up

Enclosure B includes the notes related to the set-up of the Signal Express and the routine written in Matlab.

4.4 Test's schedule

As has been said in section 2.2 the aim of this work is the characterization of the stick-slip phenomenon in a device that simplifies the Girling duo-servo brake mechanism. In order to achieve this subject a set of test has been selected. The device has several parameters. The most important are the springs stiffness and the belt's velocity. Once the parameters are selected, the following test has been made:

- A set of tests with springs with equal stiffness, 0.14 N/mm, at 5, 10, 15, 20, 25 rpm

- A set of tests with springs with equal stiffness, 0.34 N/mm, at 5, 10, 15, 20, 25 rpm
- A set of tests with springs with different stiffness, the vertical spring with 0.34 N/mm and the horizontal springs with 0.14 N/mm, at 5, 10, 15, 20, 25 rpm

The stiffness of the springs are calculated from mean coil diameter and wire diameter

$$k = \frac{d^4 \cdot G}{8 \cdot D^3 \cdot N_a} = \frac{d^4 \cdot E}{16 \cdot (1+\nu) \cdot D^3 \cdot N_a} \tag{45}$$

where d is the wire diameter, D is the mean coil diameter, Na is the coil number, E is the Young module, 210 GPa, and ν is the Poisson ratio, 0.3.

Table 2: Characteristics of the springs

Spring number	d (mm)	D (mm)	N_a	k (N/mm)
1	0.5	6.8	18.5	0.14
2	0.63	6.93	18.5	0.34

5 Results

5.1 Introduction

As has been said in section 4.4, the results of the tests has been scheduled in function of the springs' stiffness and angular velocity of the engine.

5.2 Tests set with 0.14 N/mm

5.2.1 Temporal and frequency analysis of the system

As has been scheduled in section 4.4, the results of the tests with 0.14 N/mm of stiffness springs are shown in this section. The first test is made at 19.36 rpm, close to 20 rpm. Figure 24 shows the displacement versus time for this velocity.

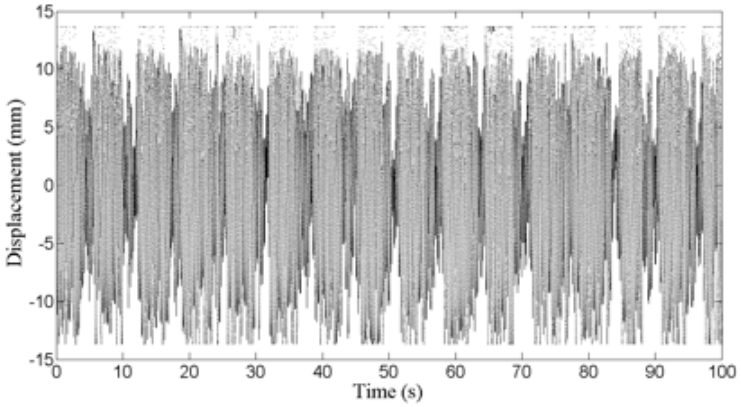

Figure 24: Displacement versus Time at 19.36 rpm

The most important remark is the appearance of pulses. To get the period of these pulses a fast Fourier transform (FFT) has been computed, Figure 25.

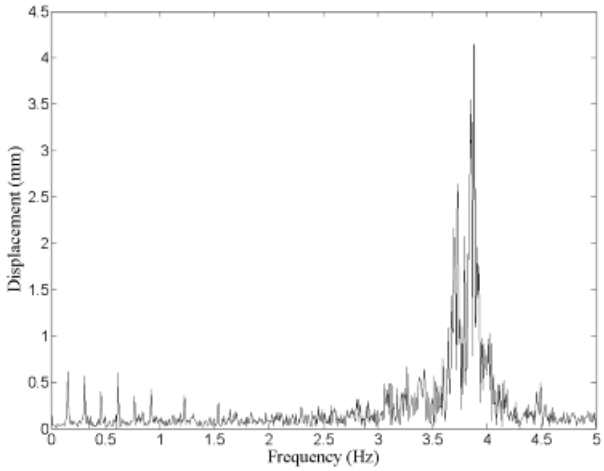

Figure 25: FFT of the displacement at 19.36 rpm

From figure 25, the first frequency is 0.1526 Hz and the correspondent period is 6.553 seconds. This value has relation with the time necessary for a belt's turn. The time for a belt turn depends on the engine velocity (n), the radius of the drums (R) and the belt's length (L):

$$T = \frac{L}{Belt's\ linear\ velocity} = \frac{L}{R \cdot n \cdot \frac{2 \cdot \pi}{60}} \tag{46}$$

Latest result means that the excitation of these pulses is the belt's velocity. The origin of this excitation is irregularities on the belt's surface, Figure 26.

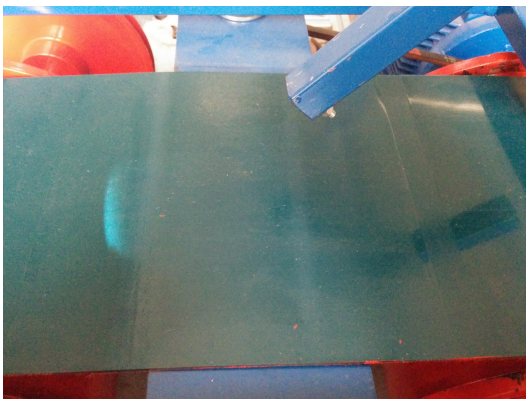

Figure 26: Picture of the overlapping joint

Another remark is that the higher displacement's peaks are cut down because of the probe measure threshold. To understand better the measure in figure 25, a zoom is made, figure 27.

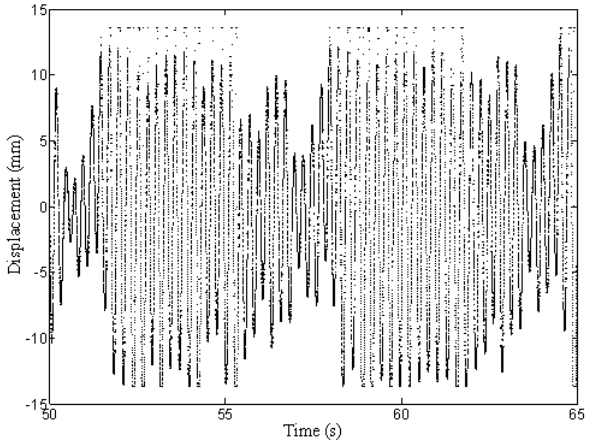

Figure 27: Zoom of figure 25

From figure 26, the highest peak has a frequency of 3.876 Hz and the correspondent period is 0.258 seconds. The natural frequency associated with a system of two degrees of freedom associated to the stiffness of the springs and the block's mass is:

$$f_n = 4.786 \text{ Hz}$$

This result comes from a calculation of the first natural frequency of the system. To accomplish this calculation it is necessary to know the stiffness of the springs and the inertial data of the components of the system: the crank mass (m_c) is 0.215 kg, and the block's mass (m) is 0.1953 kg. The length of each crank's arm is 0.105 m. The crank inertial moment (J) is calculated by:

$$J = \frac{m_c \cdot L^2}{3} \tag{47}$$

The system behaviour is represented by the following differential equations:

$$\begin{cases} m \cdot \ddot{x} + k_1 \cdot x + k_2 \cdot (x - y) = 0 \\ J \cdot \frac{\ddot{y}}{L} + k_3 \cdot y \cdot L - k_2 \cdot (x - y) \cdot L = 0 \end{cases} \tag{48}$$

Let x=x_0·sin(w·t) and y=y_0·sin(w·t), hence:

$$\begin{cases} (k_1 + k_2 - m \cdot w^2) \cdot x_0 - k_2 \cdot y_0 = 0 \\ (k_2 + k_3 - \frac{J \cdot w^2}{L^2}) \cdot y_0 - k_2 \cdot x_0 = 0 \end{cases} \tag{49}$$

Writting latest expression in matricial form:

$$\begin{bmatrix} (k_1 + k_2 - m \cdot w^2) & -k_2 \\ -k_2 & (k_2 + k_3 - \frac{J \cdot w^2}{L^2}) \end{bmatrix} \cdot \begin{bmatrix} x_0 \\ z_0 \end{bmatrix} = \begin{bmatrix} 0 \\ 0 \end{bmatrix} \tag{50}$$

Hence:

$$det(\begin{bmatrix} (k_1+k_2-m\cdot w^2) & -k_2 \\ -k_2 & (k_2+k_3-\frac{J\cdot w^2}{L^2}) \end{bmatrix}) = 0 \quad (51)$$

$$(m\cdot\frac{J}{L^2})\cdot w^4 - [(k_1+k_2)\cdot\frac{J}{L^2} - (k_2+k_3)\cdot m]\cdot w^2 + [(k_1+k_2)\cdot(k_2+k_3)] = 0 \quad (52)$$

Which gives, for sure k_1=k_2=k_3=140 $\frac{rad}{s}$ and J=0.00079012 kg$\cdot m^2$, w=30.9632 $\frac{rad}{s}$ and f=4.9279 Hz

The calculated natural frequency is different to the main frequency of the spectrum. Since this result there is no relation between natural frequency and the main frequency of the output spectrum.

Figure 28 shows a closer zoom of the figure 27. The singular block's oscillations are evident. For each oscillation the positive slope means the block getting further to the probe, in the same direction of belt's movement. Even more, the positive slope of each oscillation is on 200 mm/s and the belt's velocity is 226.66 mm/s. Thus it is possible to consider this as a slow slip.

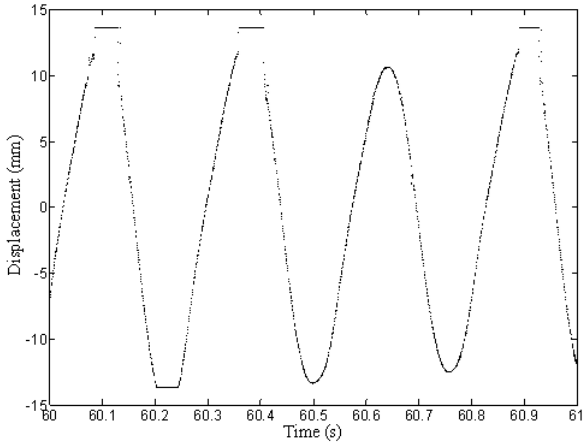

Figure 28: Closer zoom of the figure 25

The second test is made at 14.87 rpm, close to 15 rpm. Figure 29 shows the displacement versus time for this velocity.

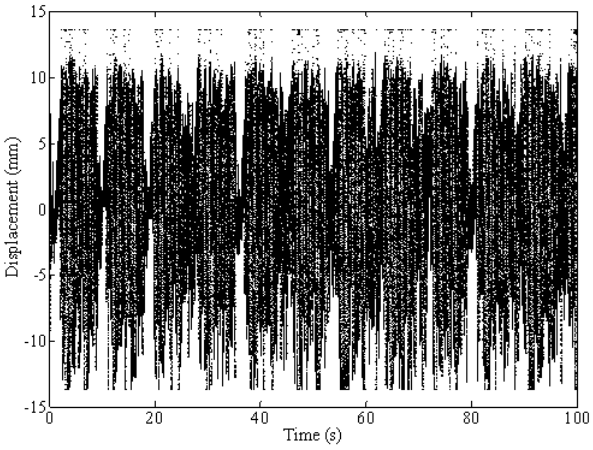

Figure 29: Displacement versus Time at 14.87 rpm

Applying the same concept of latest case, the most important remark is the appearance of pulses. To get the period of these pulses a fast Fourier transform (FFT) has been computed, Figure 30.

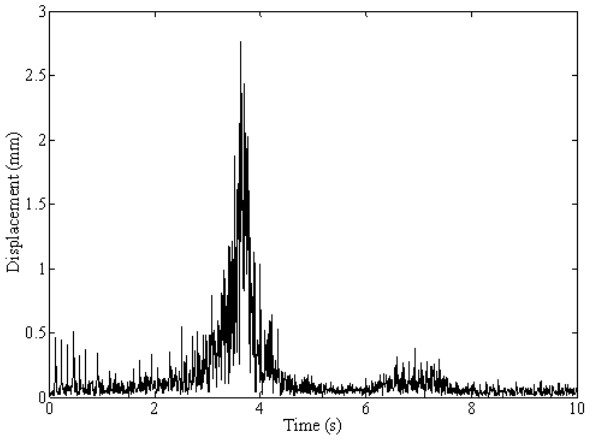

Figure 30: FFT of the displacement at 14.87 rpm

From figure 30, the first frequency is 0.1144 Hz and the correspondent period is 8.741 seconds. This value has relation with the time necessary for a belt's turn, 8.677 seconds. Latest result means that the excitation of these pulses is the belt's velocity. Another remark is that the higher displacement's peaks are cut down because of the probe measure threshold. To understand better the measure in figure 29, a zoom is made, figure 31.

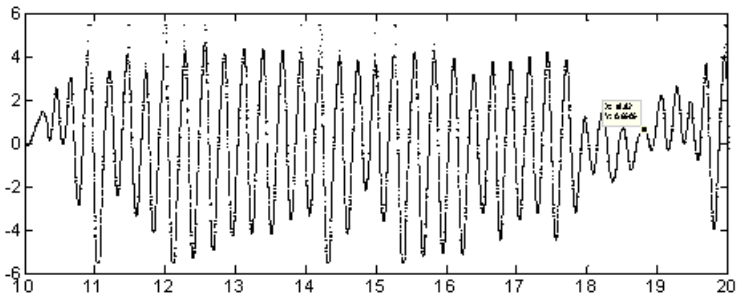

Figure 31: Zoom of figure 29

From figure 30, the highest peak has a frequency of 3.616 Hz and the correspondent period is 0.276 seconds. As has been set with the latest test, the calculated natural frequency is different to the main frequency of the spectrum. Since this result there is no relation between natural frequency and the main frequency of the output spectrum. A comparison between this main frequency and the same frequency for the latest test shows that the lower velocity the lower main frequency.

Figure 32 shows a closer zoom of the figure 31. The positive slope of each oscillation is on 160 mm/s and the belt's velocity is 174.1 mm/s. Thus it is possible to consider this as a slow slip.

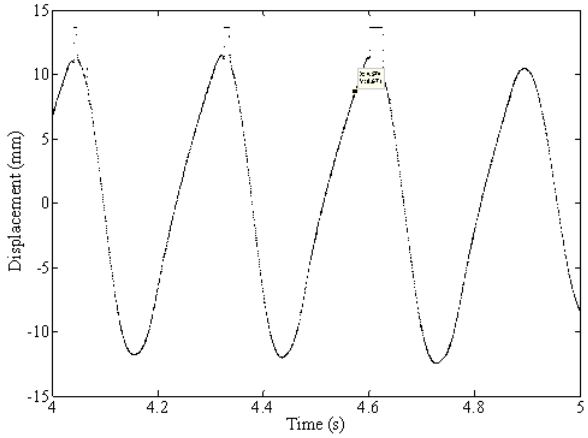

Figure 32: Closer zoom of the figure 29

The third test is made at 10.04 rpm, close to 10 rpm. Figure 33 shows the displacement versus time for this velocity.

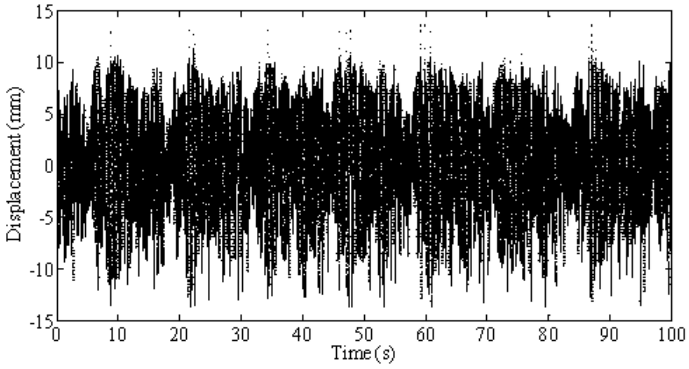

Figure 33: Displacement versus Time at 10.04 rpm

The most important remark is the appearance of pulses. To get the period of these pulses a fast Fourier transform (FFT) has been computed, Figure 34.

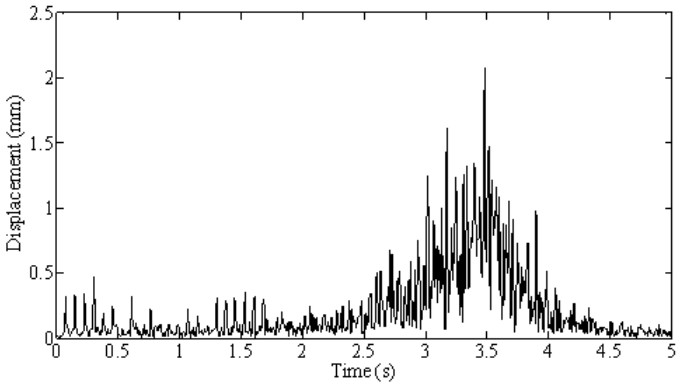

Figure 34: FFT of the displacement at 10.04 rpm

From figure 34, the first frequency is 0.07629 Hz and the correspondent period is 13.108 seconds. This value has relation with the time necessary for a belt's turn, 12.85 seconds. Latest result means that the excitation of these pulses is the belt's velocity. Another remark is that the higher displacement's peaks are cut down because of the probe measure threshold. To understand better the measure in figure 33, a zoom has been made, figure 35.

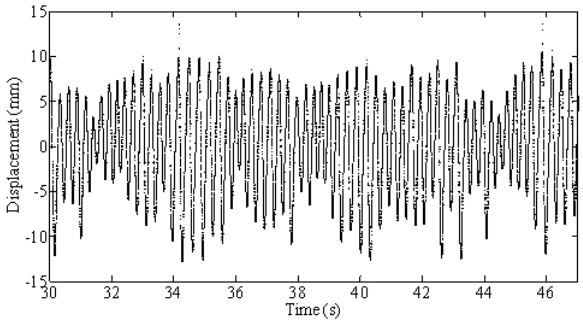

Figure 35: Zoom of figure 33

From figure 34, the highest peak has a frequency of 3.479 Hz and the correspondent period is 0.287 seconds. As has been set with the latest test, the calculated natural frequency is different to the main frequency of the spectrum. Since this result there is no relation between natural frequency and the main frequency of the output spectrum. A comparison between this main frequency and the same frequency for the latest test shows that the lower velocity the lower main frequency. Figure 36 shows a closer zoom of the figure 37. The value of positive slope of each oscillation is 117.19 mm/s and the belt's velocity is 117.545 mm/s. This result means that at this velocity a stick has been produced.

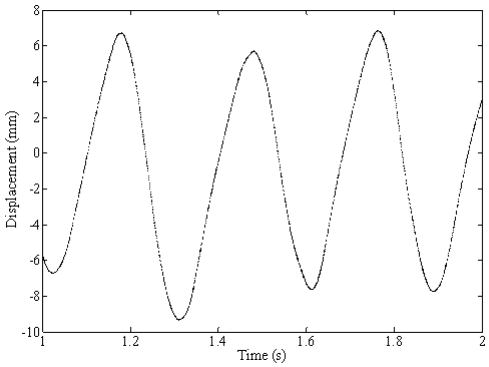

Figure 36: Closer zoom of the figure 33

Figure 37 shows the approximation between the belts velocity and the blocks velocity.

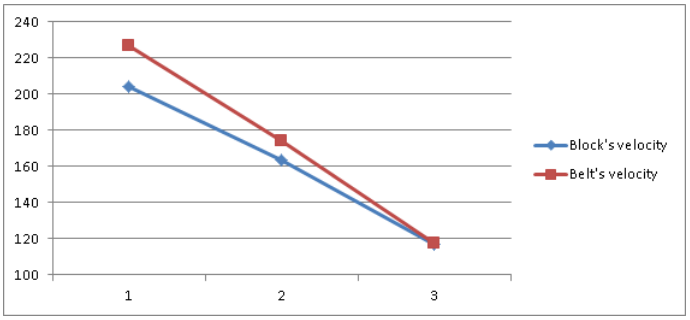

Figure 37: Comparison between the belt's and the block's velocity for the three tests

5.2.2 Phase's plane and space diagrams

In order to study the chaos of the signal a set of phase's diagrams has been developed. One of the components of this kind of diagrams is the velocity, figure 38.

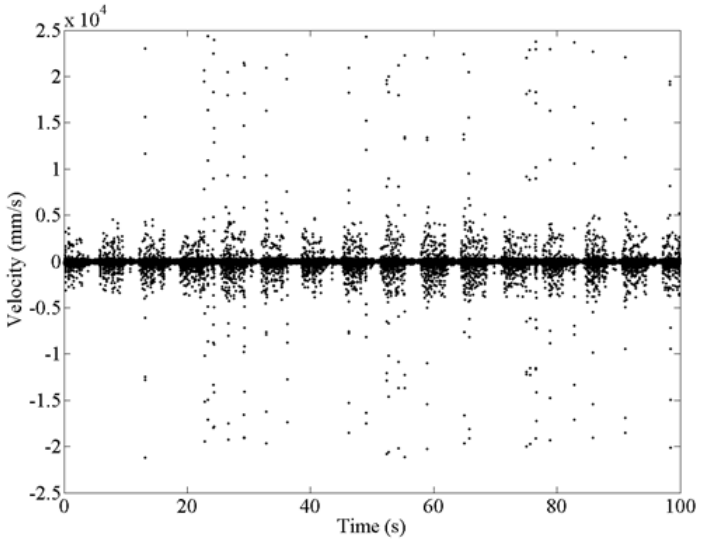

Figure 38: Evolution of the block's velocity at an angular velocity of 19.36 rpm

It is remarkable the high value of the block's velocity in a few instants, 25 m/s. An example of this high velocity value happens at 23.3 seconds, figure 39. This figure depicts a few points in a line almost vertical. The most likely cause of this discontinuity is a bad reception of the signal from the block, associated to a sudden turn of the block. To improve the chaos analysis, these discontinuities have been removed from the phase's plane and space diagrams.

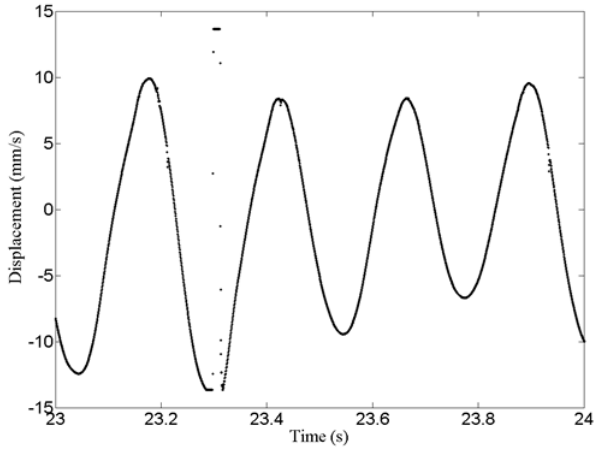

Figure 39: Evolution of displacement around 23.3 seconds

Figure 40 shows phase's plane diagram corresponding to a test at an angular velocity of 19.36 rpm.

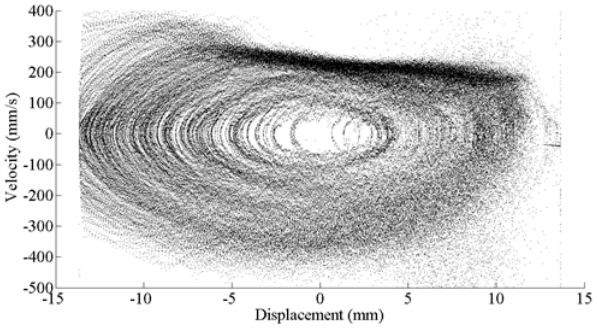

Figure 40: Phase's plane diagram for a test at an angular velocity of 19.36 rpm

Figure 41 shows phase's space diagram for the same test. The differences among the whirls inside of the column show the non-periodic behaviour of the system.

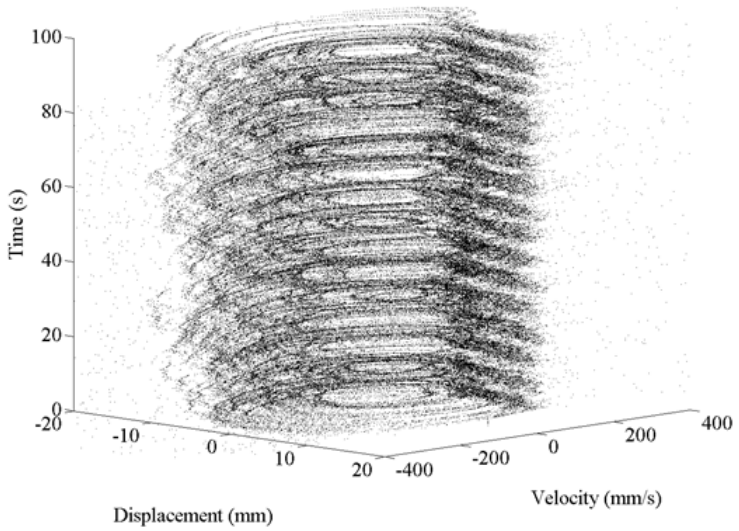

Figure 41: Phase's space diagram for a test at an angular velocity of 19.36 rpmm

Figure 42 shows phase's plane diagram corresponding to a test at an angular velocity of 14.86 rpm.

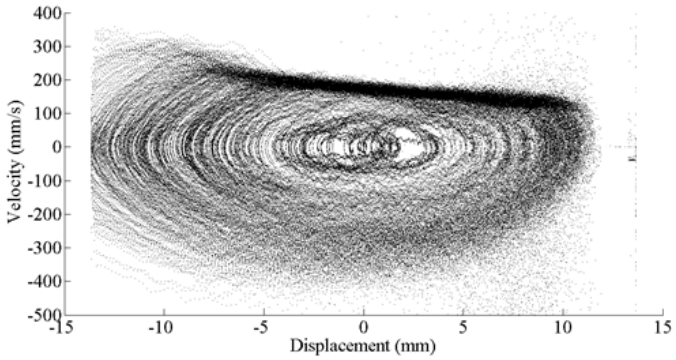

Figure 42: Phase's plane diagram for a test at an angular velocity of 14.86 rpm

Figure 43 shows phase's plane diagram corresponding to a test at an angular velocity of 10.03 rpm.

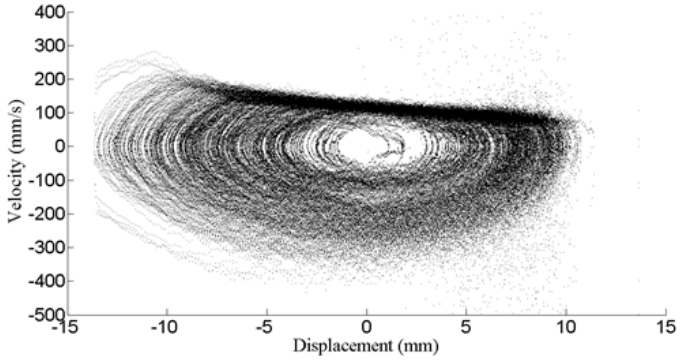

Figure 43: Phase's plane diagram for a test at an angular velocity of 10.03 rpm

Figure 44 shows phase's space diagram for the same test. The small differences among the whirls inside of the column show a more periodical behaviour of the system than in the figure 41.

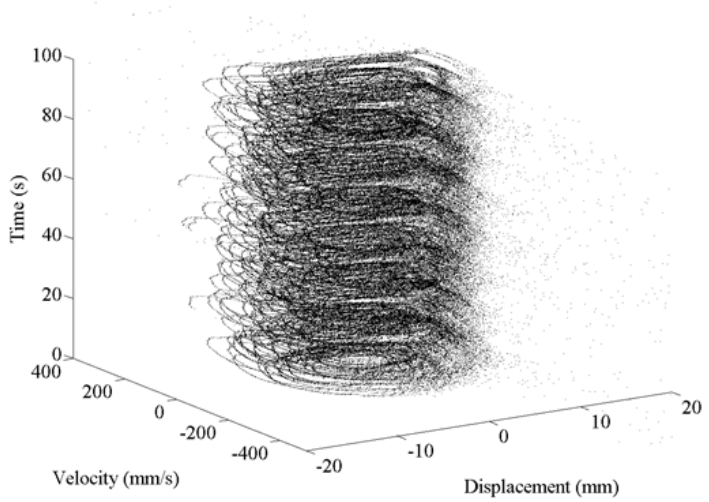

Figure 44: Phase's space diagram for a test at an angular velocity of 10.03 rpm

The boundaries of these phase's plane diagrams are similar, with an upper side which is represented by a straight line with a light slope. A horizontal line means constant velocity, in the case in which this constant velocity is the same that the belt's linear velocity, the block is stuck. Thus, from figure 40, the velocity is close to 226.66 mm/s, the belts linear velocity at 19.36 rpm. Similarly, from figure 42 the velocity is close to 173.97 mm/s, the belts linear velocity at 14.86 rpm, and from figure 43 the velocity is close to 113.33 mm/s, the belts linear velocity at 10.03 rpm. The higher the angular velocity is, the greater displacement range is, and the same behaviour is found for the velocity range

5.3 Tests set with 0.34 N/mm

5.3.1 Temporal and frequency analysis of the system

As has been scheduled in section 4.4, the results of the tests with 0.34 N/mm of stiffness springs are shown in this section. The first test is made at 19.36 rpm, close to 20 rpm. Figure 45 shows the displacement versus time for this velocity.

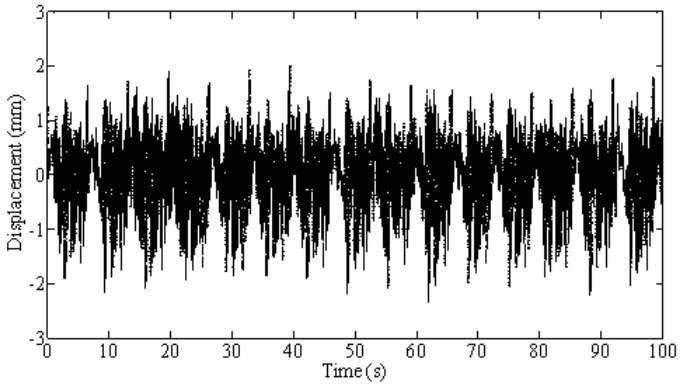

Figure 45: Displacement versus time at 19.36 rpm

The most important remark is the appearance of pulses. To get the period of these pulses a fast Fourier transform (FFT) has been computed, Figure 46.

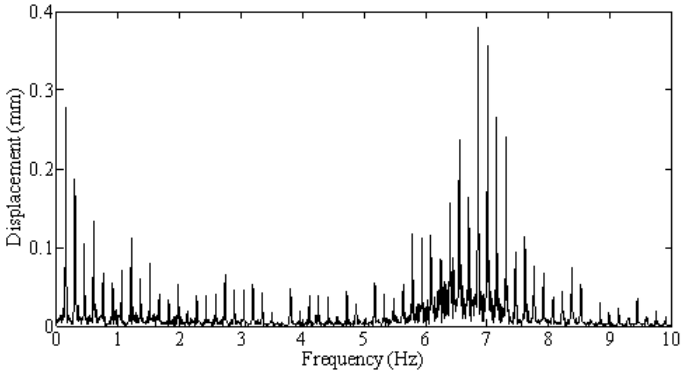

Figure 46: FFT of the displacement at 19.36 rpm

From figure 46, the first frequency is 0.1526 Hz and the correspondent period is 6.553 seconds. This value has relation with the time necessary for a belt's turn, 6.664 seconds. Latest result means that the excitation of these pulses is the belt's velocity. To understand better the measure in figure 45, a zoom is made, figure 47.

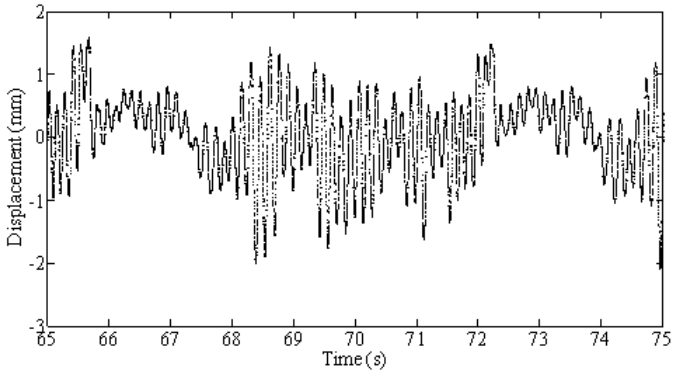

Figure 47: Zoom of figure 45

From figure 45, the highest peak has a frequency of 6.851 Hz and the correspondent period is 0.146 seconds. The natural frequency associated with a system of two degrees of freedom associated to the stiffness of the springs and the block's mass is:

$$f_n = 4.9279 \text{ Hz}$$

This result comes from a calculation of the first natural frequency of the system. To accomplish this calculation only it is necessary to change the value of the stiffness of all the springs. The calculated natural frequency is different to the main frequency of the spectrum. Since this result there is no relation between natural frequency and the main frequency of the output spectrum.

A comparison between figure 25 with figure 46. The main remark is that for sure the higher stiffness the lower amplitude. Even more, the frequency bandwidth in figure 45 from 5.5 to 7.5 Hz is less chaotic than the correspondent in figure 27 from 3.5 to 4 Hz.

Figure 48 shows a closer zoom of the figure 45. The positive slope of each oscillation is on 36 mm/s and the belt's velocity is 226.6 mm/s. Thus it is possible to consider this as a clear slip.

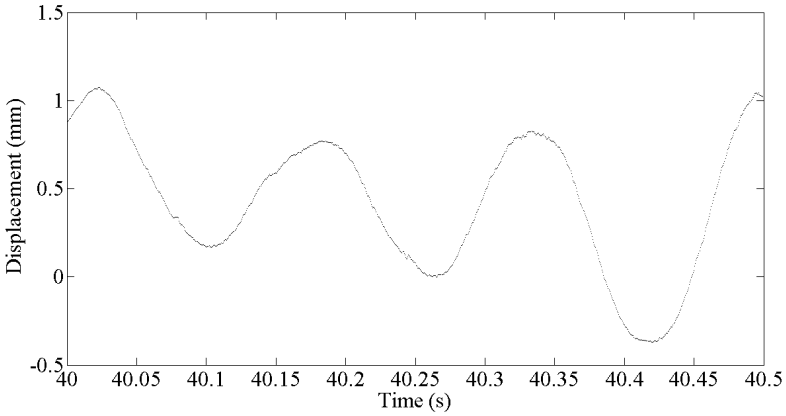

Figure 48: Closer zoom of the figure 45

The second test is made at 14.87 rpm, close to 15 rpm. Figure 49 shows the displacement versus time for this velocity.

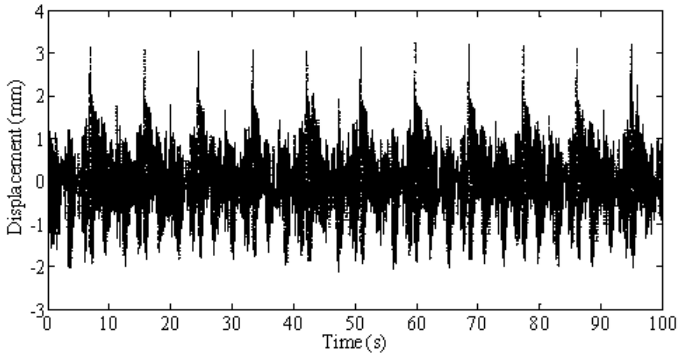

Figure 49: Displacement versus time at 14.87 rpm

The most important remark is the appearance of pulses. To get the period of these pulses a fast Fourier transform (FFT) has been computed, Figure 50.

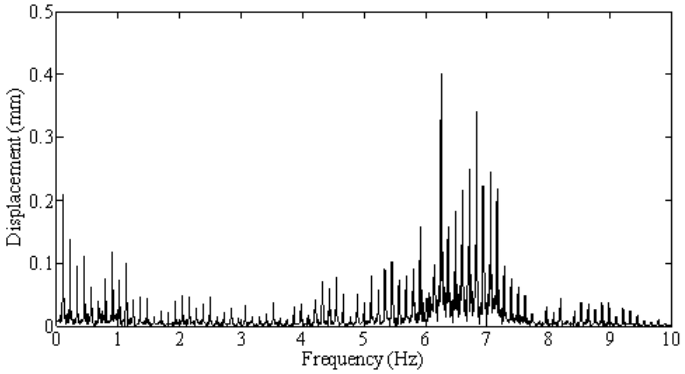

Figure 50: FFT of the displacement at 14.87 rpm

From figure 50, the first frequency is 0.1144 Hz and the correspondent period is 8.741 seconds. This value has relation with the time necessary for a belt's turn, 8.677 seconds. Latest result means that the excitation of these pulses is the belt's velocity.

To understand better the measure in figure n, a zoom is made, figure 51.

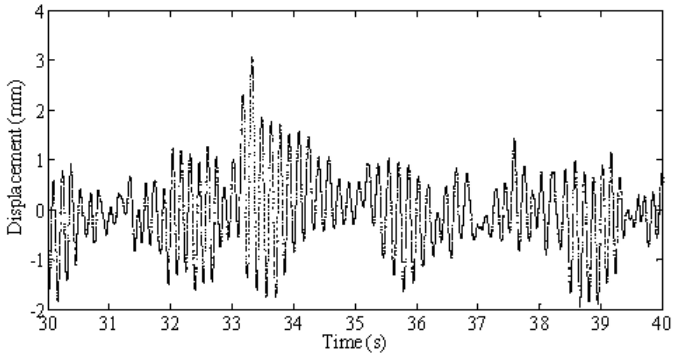

Figure 51: Zoom of figure 49

From figure 50, the highest peak has a frequency of 6.256 Hz and the correspondent period is 0.159 seconds. As has been set with the latest test, the calculated natural frequency is different to the main frequency of the spectrum. Since this result there is no relation between natural frequency and the main frequency of the output spectrum. Figure 52 shows a closer zoom of the figure 49. The positive slope of each oscillation is on 42 mm/s and the belt's velocity is 174.1 mm/s. Thus it is possible to consider this as a clear slip.

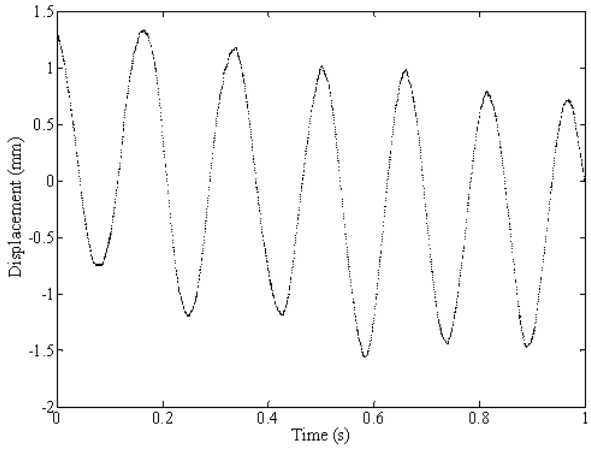

Figure 52: Closer zoom of the figure 49

The third test is made at 10.04 rpm, close to 10 rpm. Figure 53 shows the displacement versus time for this velocity.

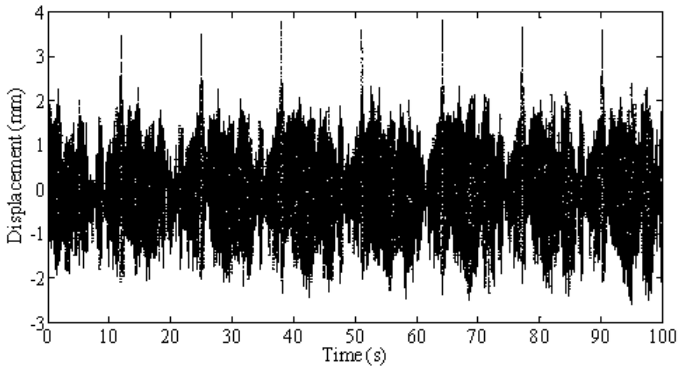

Figure 53: Displacement versus time at 10.04 rpm

The most important remark is the appearance of pulses. To get the period of these pulses a fast Fourier transform (FFT) has been computed, Figure 54.

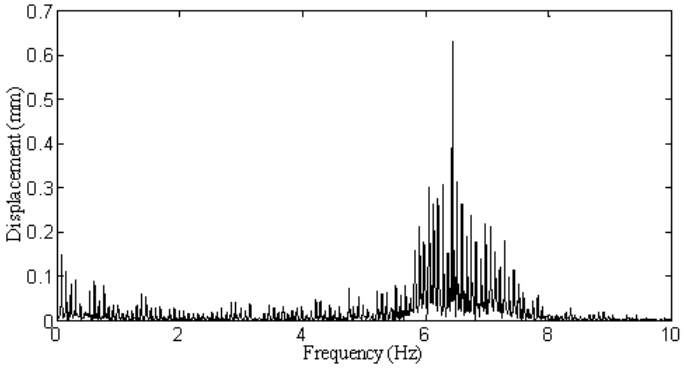

Figure 54: FFT of displacement at 10.04 rpm

From figure 53, the first frequency is 0.07629 Hz and the correspondent period is 13.108 seconds. This value has relation with the time necessary for a belt's turn, 12.85 seconds. Latest result means that the excitation of these pulses is the belt's velocity.

To understand better the measure in figure 53, a zoom has been made, figure 55.

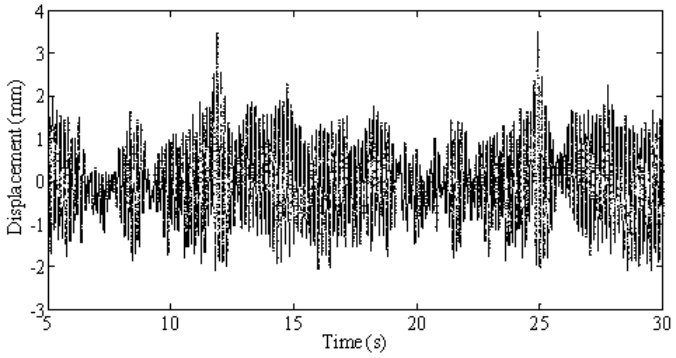

Figure 55: Zoom of figure 53

From figure 54, the highest peak has a frequency of 6.439 Hz and the correspondent period is 0.155 seconds. As has been set with the latest test, the calculated natural frequency is different to the main frequency of the spectrum. Since this result there is no relation between natural frequency and the main frequency of the output spectrum.

Figure 56 shows a closer zoom of the figure 53. The positive slope of each oscillation is on 43 mm/s and the belt's velocity is 117.2 mm/s. Thus it is possible to consider this as a clear slip.

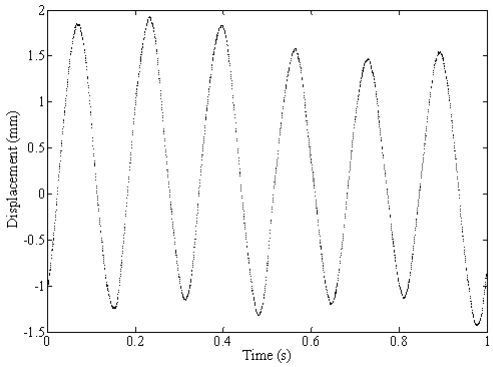

Figure 56: Closer zoom of the figure 53

The last test is made at 4.87 rpm, close to 5 rpm. Figure 57 shows the displacement versus time for this velocity.

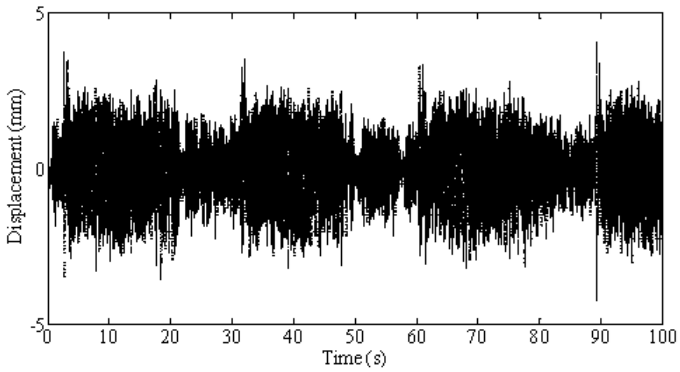

Figure 57: Displacement versus time at 4.87 rpm

The most important remark is the appearance of pulses. To get the period of these pulses a fast Fourier transform (FFT) has been computed, Figure 58.

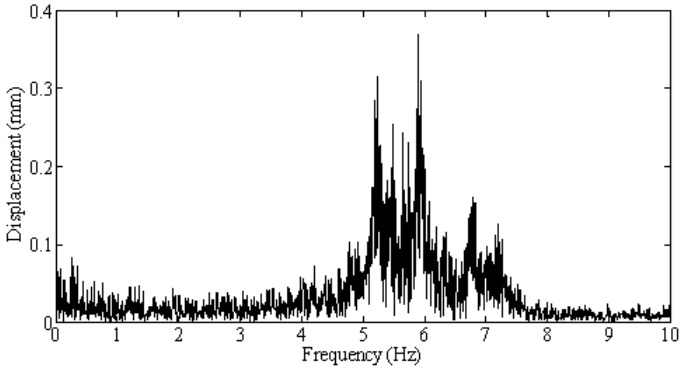

Figure 58: FFT of displacement at 4.87 rpm

From figure 58, the first frequency is 0.03815 Hz and the correspondent period is 26.212 seconds. This value has relation with the time necessary for a belt's turn, 26.491 seconds. Latest result means that the excitation of these pulses is the belt's velocity.

To understand better the measure in figure 57, a zoom is made, figure 59.

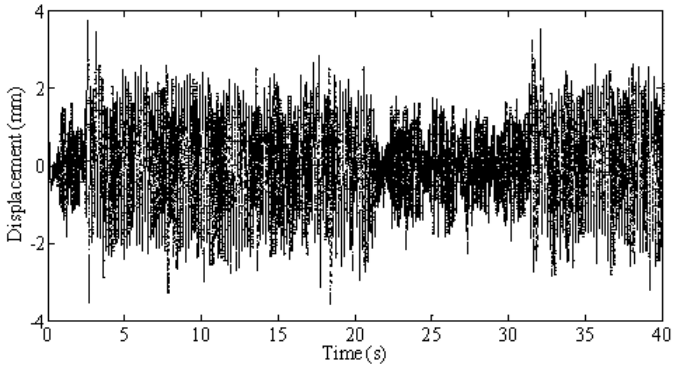

Figure 59: Zoom of figure 57

From figure 58, the highest peak has a frequency of 5.898 Hz and the correspondent period is 0.169 seconds. As has been set with the latest test, the calculated natural frequency is different to the main frequency of the spectrum. Since this result there is no relation between natural frequency and the main frequency of the output spectrum.

Figure 60 shows a closer zoom of the figure 57. The positive slope of each oscillation is on 48 mm/s and the belt's velocity is 57.01 mm/s. Thus it is possible to consider this as a slow slip.

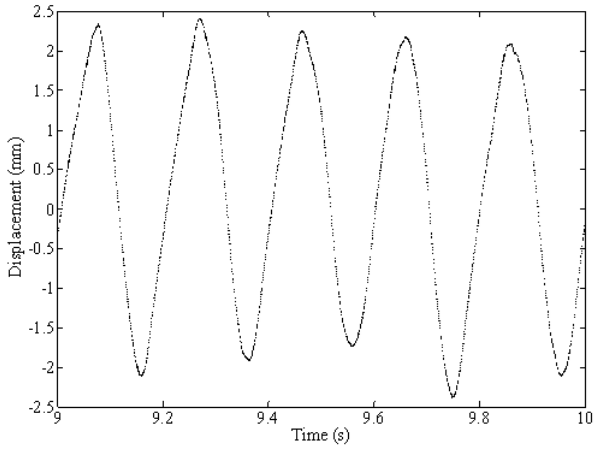

Figure 60: Closer zoom of the figure 57

Figure 61 shows the evolution of the main frequency versus the belt's turn frequency. The most important remark is the change of the slope of the curve.

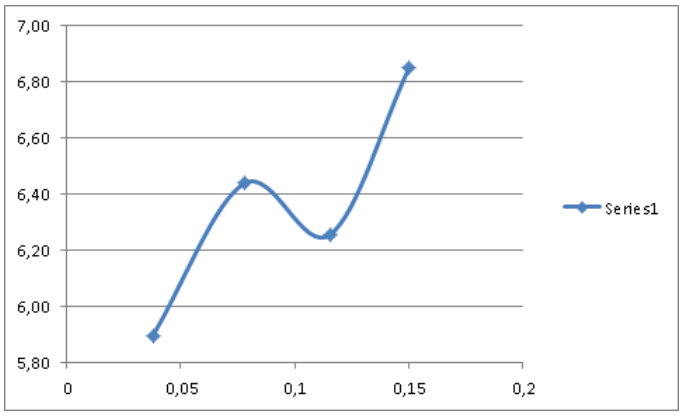

Figure 61: Main frequency versus belt's turn frequency

5.3.2 Phase's plane and space diagrams

In order to study the chaos of the signal a set of phase's diagrams has been developed. One of the components of this kind of diagrams is the velocity, figure 62.

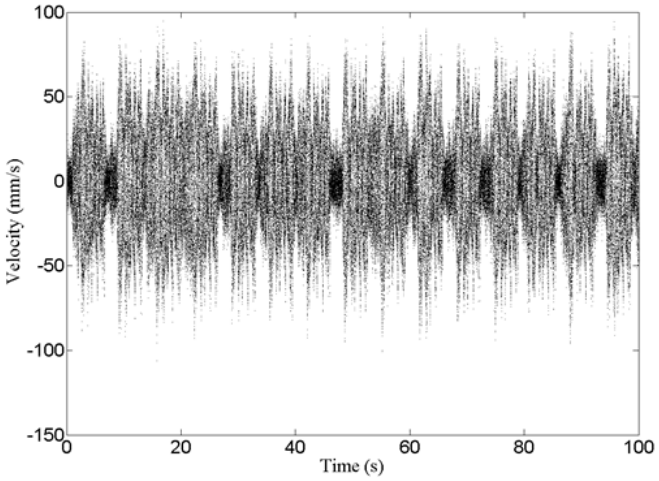

Figure 62: Evolution of the block's velocity at an angular velocity of 19.36 rpm

In this test the velocity values are more reasonable, without discontinuities. Figure 63 shows phase's plane diagram corresponding to a test at an angular velocity of 19.36 rpm.

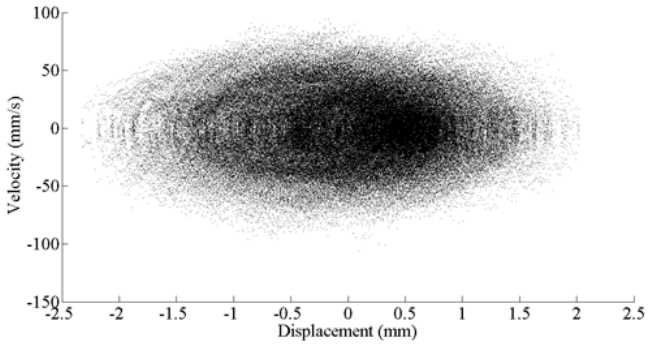

Figure 63: Phase's plane diagram for a test at an angular velocity of 19.36 rpm

Figure 64 shows phase's space diagram for the same test. It is not possible recognize any regularity.

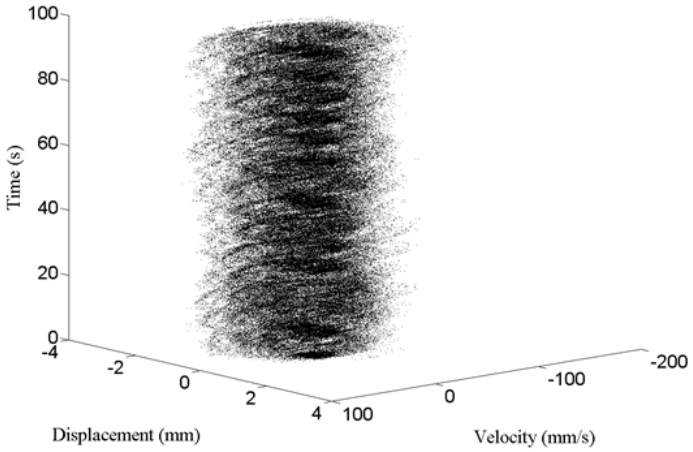

Figure 64: Phase's space diagram for a test at an angular velocity of 19.36 rpm

Figure 65 shows phase's plane diagram corresponding to a test at an angular velocity of 14.86 rpm.

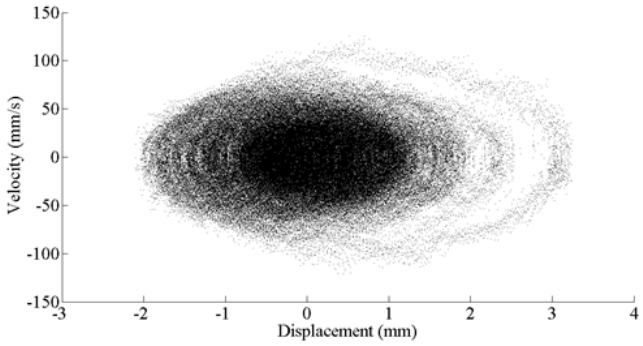

Figure 65: Phase's plane diagram for a test at an angular velocity of 14.86 rpm

Figure 66 shows phase's plane diagram corresponding to a test at an angular velocity of 10.03 rpm.

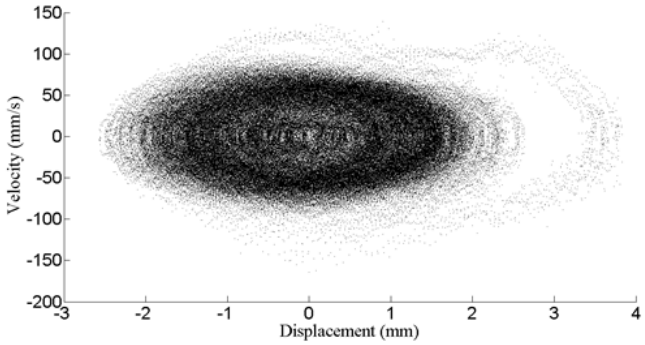

Figure 66: Phase's plane diagram for a test at an angular velocity of 10.03 rpm

Figure 67 shows phase's plane diagram corresponding to a test at an angular velocity of 4.47 rpm.

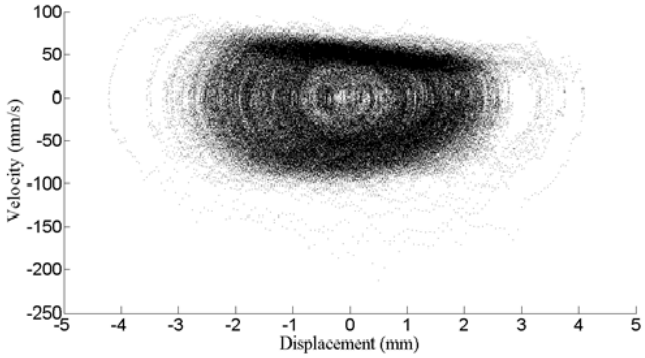

Figure 67: Phase's plane diagram for a test at an angular velocity of 4.47 rpm

Figure 68 shows phase's space diagram for the same test. The small differences among the whirls inside of the column show a more periodical behaviour of the system than in the figure 64.

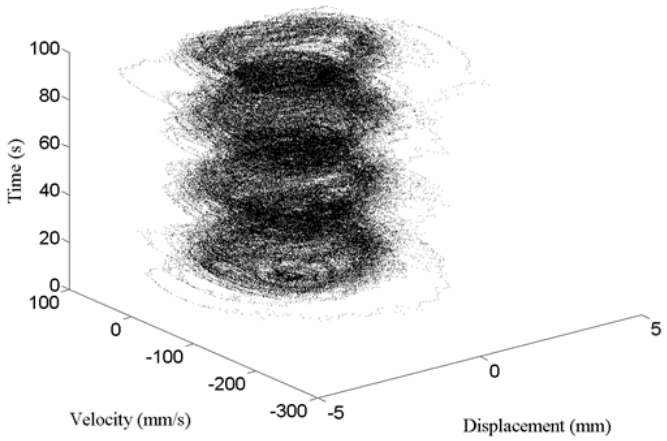

Figure 68: Phase's space diagram for a test at an angular velocity of 4.47 rpm

The boundaries of the three first phase's plane diagrams are similar, whereas the fourth phase's plane diagram has an upper boundary which is represented by a straight line with a light slope. The explanation of the straight line is the mentioned in 5.2.1.

The higher the angular velocity is greater displacement range is too. The test at 20 rpm has the smaller block's velocity range. This is due to very high belt's velocity, which improves smooth slip behaviour. In other tests, the higher the angular velocity is greater block's velocity range is.

The tests with lower belt's velocity have a halo at the right side. The test with 14.87 rpm has the halos periodically distributed, with a period of 8.8 seconds, close to the belt's turn period. Thus the most likely cause of these halos is one of the belt's joints, figure 26.

5.4 Tests set with both kind of springs

5.4.1 Temporal and frequency analysis of the system

The unique test made with this spring configuration was at 4.87 rpm. Displacement versus time is represented in Figure 69.

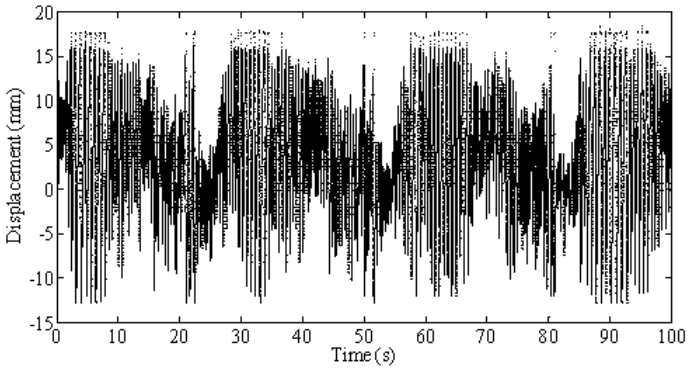

Figure 69: Displacement versus time at 4.87 rpm

The most important remark is the appearance of pulses. To get the period of these pulses a fast Fourier transform (FFT) has been computed, Figure 70.

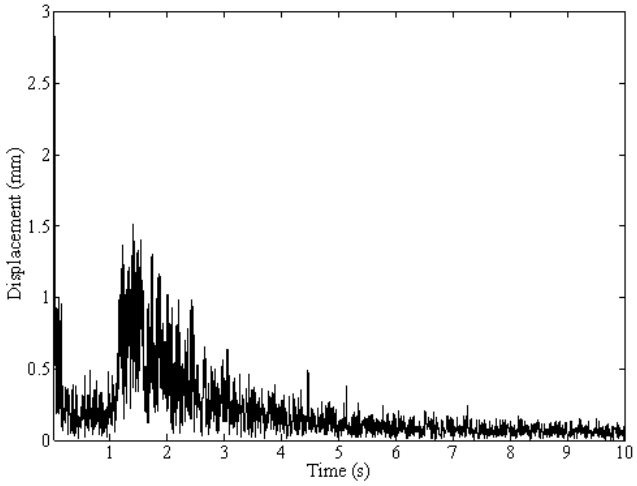

Figure 70: FFT of the displacement at 4.87 rpm

The time necessary for a belt's turn, 26.491 seconds which corresponds to a frequency of value 0.03434 Hz. This frequency is very low to be appreciated in figure 70. In order to test the presence of this frequency a zoom of the spectrum

has been made in figure 71. This frequency matches with the main frequency in this spectrum, 0.03434 Hz. Latest result means that the excitation of these pulses is the belt's velocity.

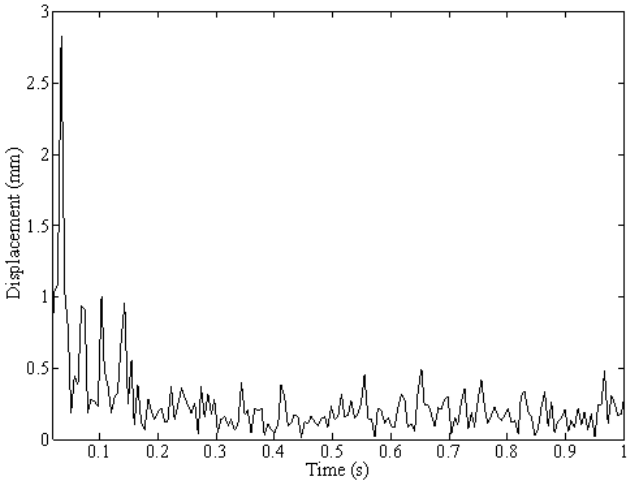

Figure 71: Zoom of FFT

From figure 71, the first frequency is 0.03434 Hz and the correspondent period is 26.212 seconds. This value has relation with the time necessary for a belt's turn, 26.491 seconds. Another remark is that the higher displacement's peaks are cut down because of the probe measure threshold. To understand better the measure in figure 69, a zoom is made, figure 72.

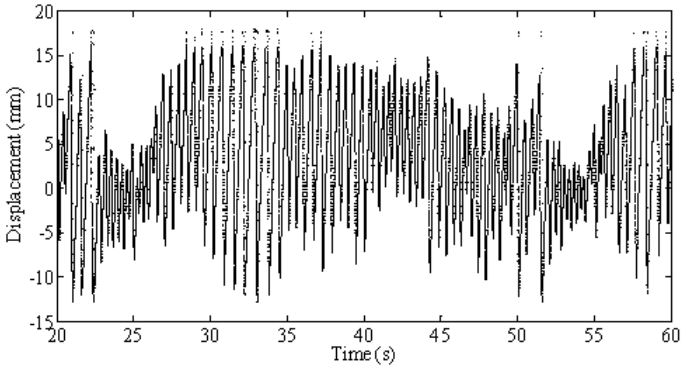

Figure 72: Zoom of figure 69

Figure 73 shows a closer zoom of figure 69. The positive slope of each oscillation is on 49 mm/s and the belt's velocity is 52 mm/s. The figure shows clearly

a stick phenomenon. The difference between the belt's velocity, about 3 mm/s is due to the instability of the belt's velocity that can explain the value of 49 instead of 52 mm/s measures at the begin of the test.

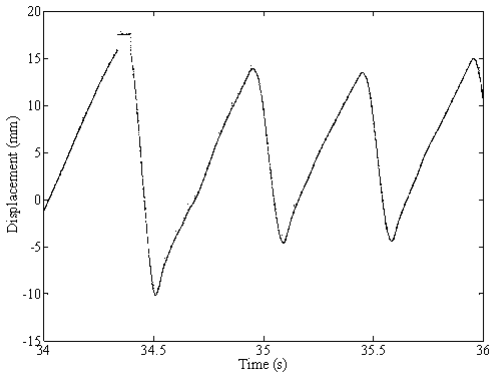

Figure 73: Closer zoom of figure 69

5.4.2 Phase's plane and space diagrams

In order to study the chaos of the signal a set of phase's diagrams has been developed. One of the components of this kind of diagrams is the velocity, figure 77.

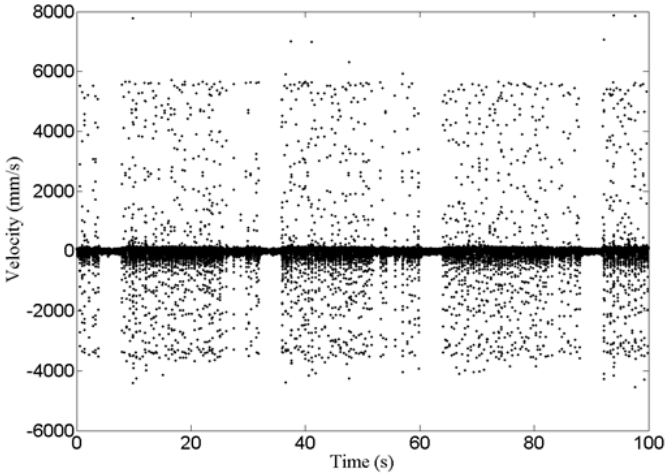

Figure 74: Evolution of the block's velocity at an angular velocity of 4.87 rpm

It is remarkable the high value of the block's velocity in a few instants, 5.7 m/s. An example of this high velocity value happens at 70.4 seconds, figure 75.

This figure depicts a few points in a line almost vertical. As has been said, the most likely cause of this discontinuity is a bad reception of the signal from the block, associated to a sudden turn of the block.

To improve the chaos analysis, these discontinuities have been removed from the phase's plane diagrams.

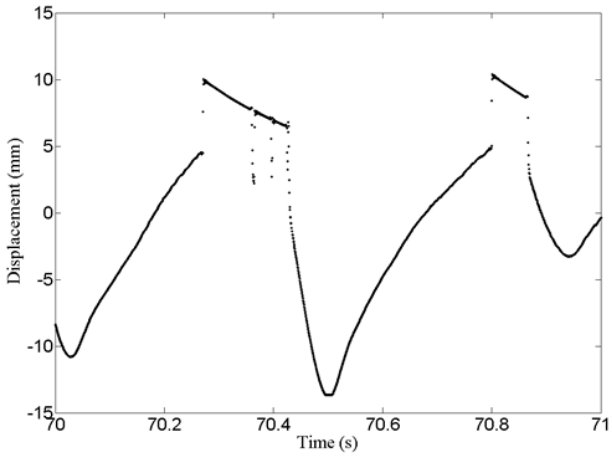

Figure 75: Evolution of displacement around 70.4 seconds

Figure 76 shows phase's plane diagram corresponding to a test at an angular velocity of 4.87 rpm.

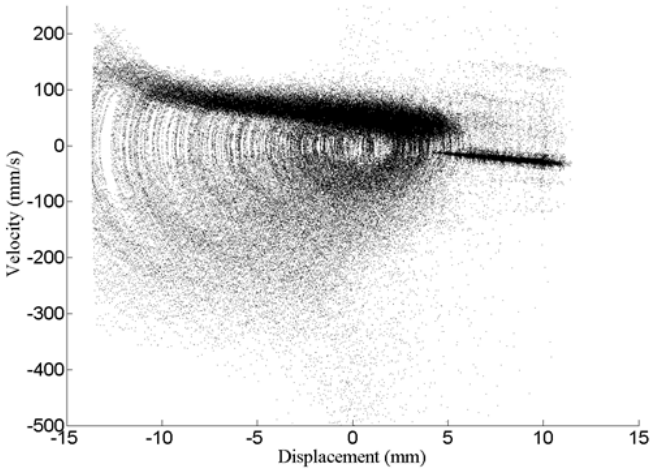

Figure 76: Phase's plane diagram for a test at an angular velocity of 4.87 rpm

The boundary of this phase's plane diagram has an upper side which is rep-

resented by two straight lines with a light slope. The left straight line, close to 50 mm/s at the middle, has relation with the belt's velocity, 52.33 mm/s. The right straight line, near to -20 mm/s which is associated with the block's bouncing movement related to the springs.

Conclusions

A test of a device equivalent to a Girling duo-servo brake mechanism has been made. The main result is the characterization of a series of frequency associated to the system. The frequency in the spectrum that matches with the belt's turn frequency is the clearest relation response excitation. The excitation source is related to two small notches on the surface of the belt. A frequency bandwidth with a main frequency, which has no relation to the natural frequencies of the system, is present in each spectrum and is related to non-linear friction phenomenon.

Several probes have been studied to find the best solution, which is obtained with the laser distance sensor. Even using this sensor, the block's displacement in the workbench is greater than the probe's measure threshold in some assemblies. Several belts have been tested and the belt with smoother notches has been selected. Another source of instability comes from the necessary velocities used in the test. These force the electric motor to run at very low velocity that produces instabilities that has been considered in the analysis results. Amid the recommendations, it would be suitable get a belt without notches and another driver.

In the present work the following tests has been developed with three springs set. With a set of 0.14 N/mm stiffness springs, tests have been completed at 20, 15 and 10 rpm. With a set of 0.34 N/mm stiffness springs, tests have been completed at 20, 15, 10 and 5 rpm. With a set of 0.14 and 0.34 N/mm, a test has been completed at 5 rpm.

For measures related to the set of 0.14 N/mm stiffness springs, the lower angular velocity is, the more chaotic the system's behaviour is. For measures related to the set of 0.34 N/mm stiffness springs, the higher angular velocity is, the more chaotic the system's behaviour is. For the measure related to the set of hybrid springs, the phase's plane space shows an area which has not relation to stick phenomenon owing to a negative slope, instead of the positive slope associated to the stick. A comparison of the results at 10 rpm for both kinds of springs sets, 0.14 and 0.34 N/mm, shows the stiffer springs are, the more chaotic behaviour is.

Expression of thanks

On reaching this important stage, is when I want to express my thanks to everyone involved in this project. Not forgetting my family to whom I owe everything.

Special thanks to Dr. José Andrés Moreno Nicolás, Dr. Pedro Adolfo Meroño Pérez and Dr. Pentxo Marín García for letting me to learn from their knowledge, and their sincere intervention to help me to complete this work.

Enclosure

Enclosure 1: Planes of the system

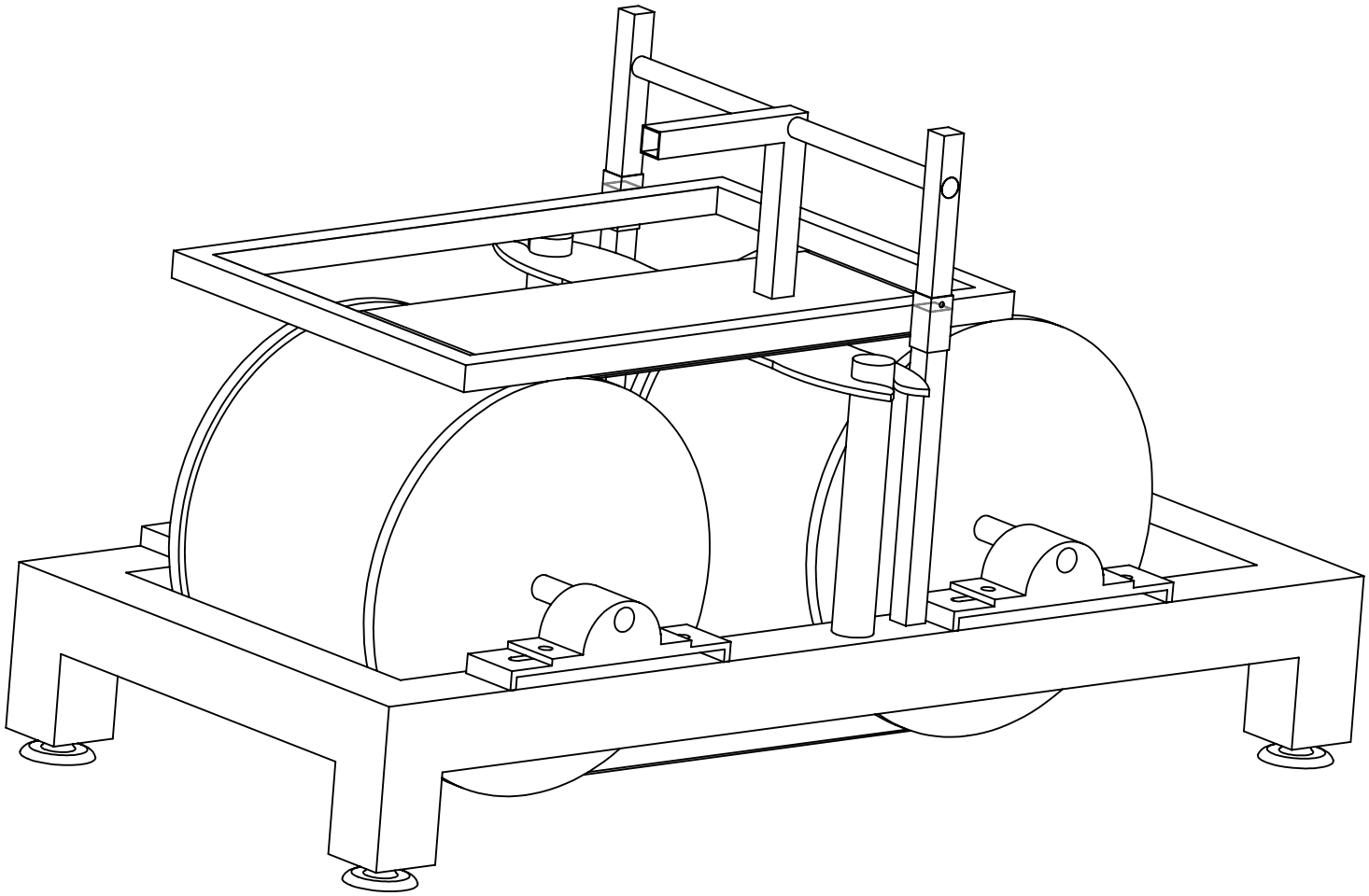

ESCALA 1 : 5

SI NO SE INDICA LO CONTRARIO: LAS COTAS SE EXPRESAN EN MM ACABADO SUPERFICIAL: TOLERANCIAS: LINEAL: ANGULAR:	ACABADO:	REBARBAR Y ROMPER ARISTAS VIVAS	NO CAMBIE LA ESCALA / REVISIÓN

	NOMBRE	FIRMA	FECHA
DIBUJ.			
VERIF.			
APROB.			
FABR.			
CALID.			

TÍTULO:

Assembly

MATERIAL:

PESO:

N.º DE DIBUJO

GDSBMAP

A4

ESCALA:1:20

HOJA 1 DE 1

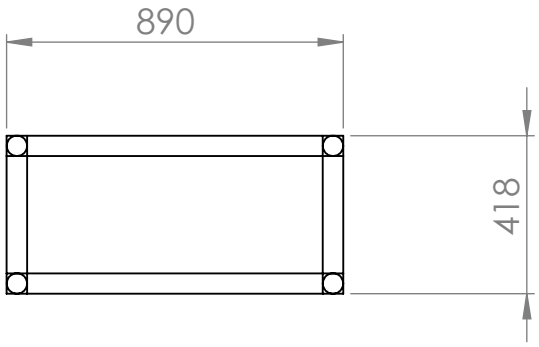

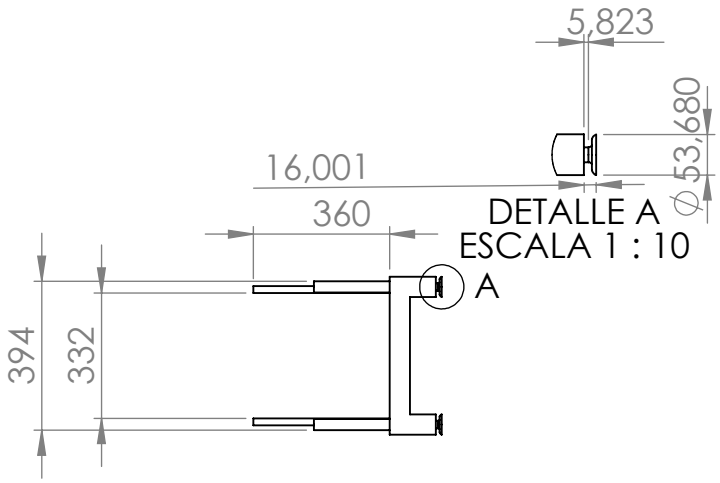

DETALLE A
ESCALA 1 : 10

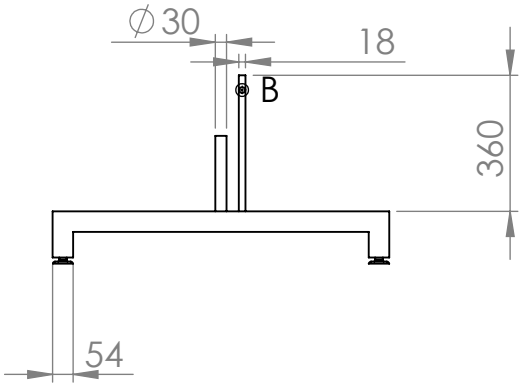

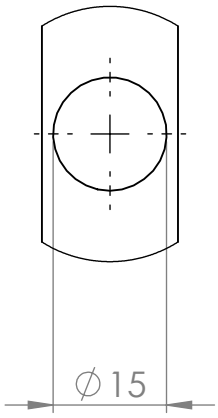

DETALLE B
ESCALA 1 : 1

UNLESS OTHERWISE SPECIFIED: DIMENSIONS ARE IN MILLIMETERS SURFACE FINISH: TOLERANCES: LINEAR: ANGULAR:		FINISH:		DEBUR AND BREAK SHARP EDGES	DO NOT SCALE DRAWING	REVISION
	NAME	SIGNATURE	DATE		TITLE: Frame	
DRAWN						
CHK'D						
APPV'D						
MFG						
Q.A				MATERIAL:	DWG NO. GDSBMAF	A4
				WEIGHT:	SCALE:1:20	SHEET 1 OF 1

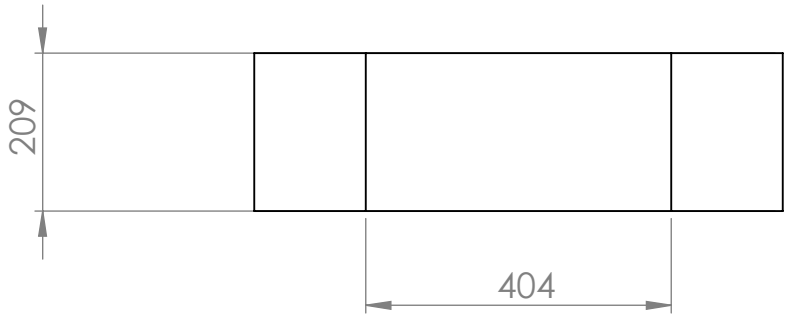

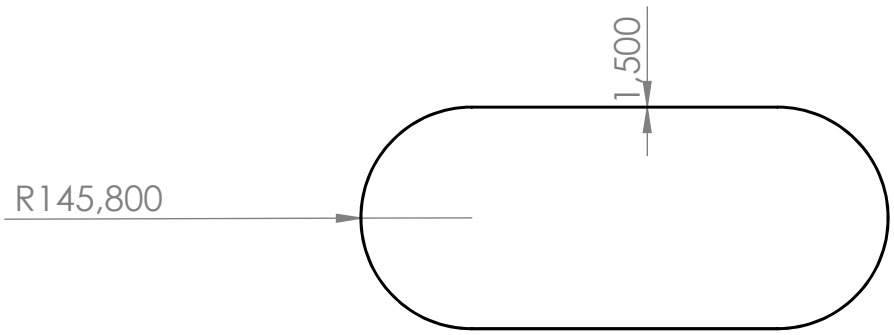

UNLESS OTHERWISE SPECIFIED: DIMENSIONS ARE IN MILLIMETERS SURFACE FINISH: TOLERANCES: LINEAR: ANGULAR:	FINISH:		DEBUR AND BREAK SHARP EDGES		DO NOT SCALE DRAWING	REVISION
	NAME	SIGNATURE	DATE		TITLE: Belt	
DRAWN						
CHK'D						
APPV'D						
MFG						
Q.A				MATERIAL:	DWG NO. GDSBMB	A4
				WEIGHT:	SCALE:1:10	SHEET 1 OF 1

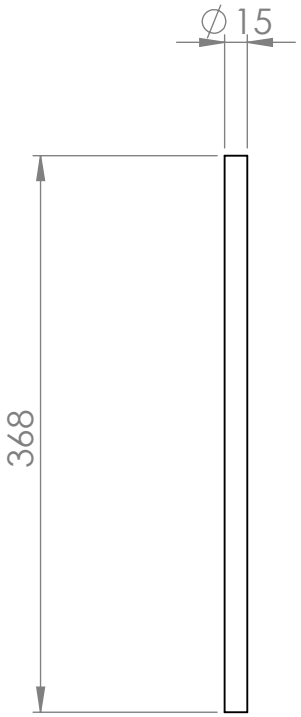

UNLESS OTHERWISE SPECIFIED: DIMENSIONS ARE IN MILLIMETERS SURFACE FINISH: TOLERANCES: LINEAR: ANGULAR:	FINISH:		DEBUR AND BREAK SHARP EDGES		DO NOT SCALE DRAWING	REVISION
	NAME	SIGNATURE	DATE		TITLE: Crank's bar	
DRAWN						
CHK'D						
APPV'D						
MFG						
Q.A				MATERIAL:	DWG NO. GDSBMBC	A4
				WEIGHT:	SCALE:1:5	SHEET 1 OF 1

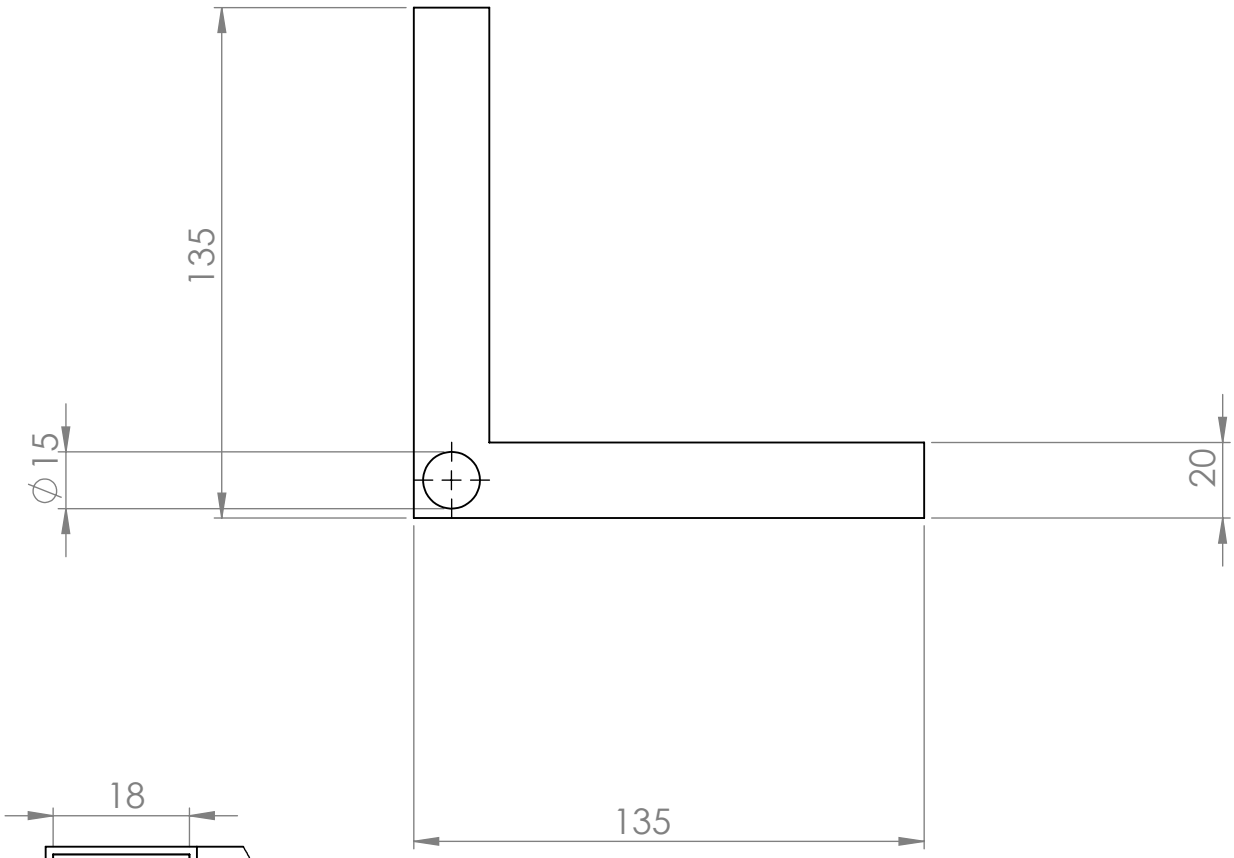

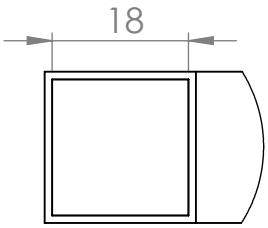

DETALLE A
ESCALA 1 : 1

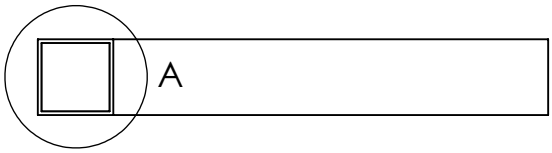

SI NO SE INDICA LO CONTRARIO: LAS COTAS SE EXPRESAN EN MM ACABADO SUPERFICIAL: TOLERANCIAS: LINEAL: ANGULAR:	ACABADO:		REBARBAR Y ROMPER ARISTAS VIVAS	NO CAMBIE LA ESCALA	REVISIÓN	
	NOMBRE	FIRMA	FECHA			
DIBUJ.						
VERIF.						
APROB.						
FABR.						
CALID.				MATERIAL:		
				PESO:		

TÍTULO:

Crank

N.º DE DIBUJO

GDSBMC

A4

ESCALA:1:2

HOJA 1 DE 1

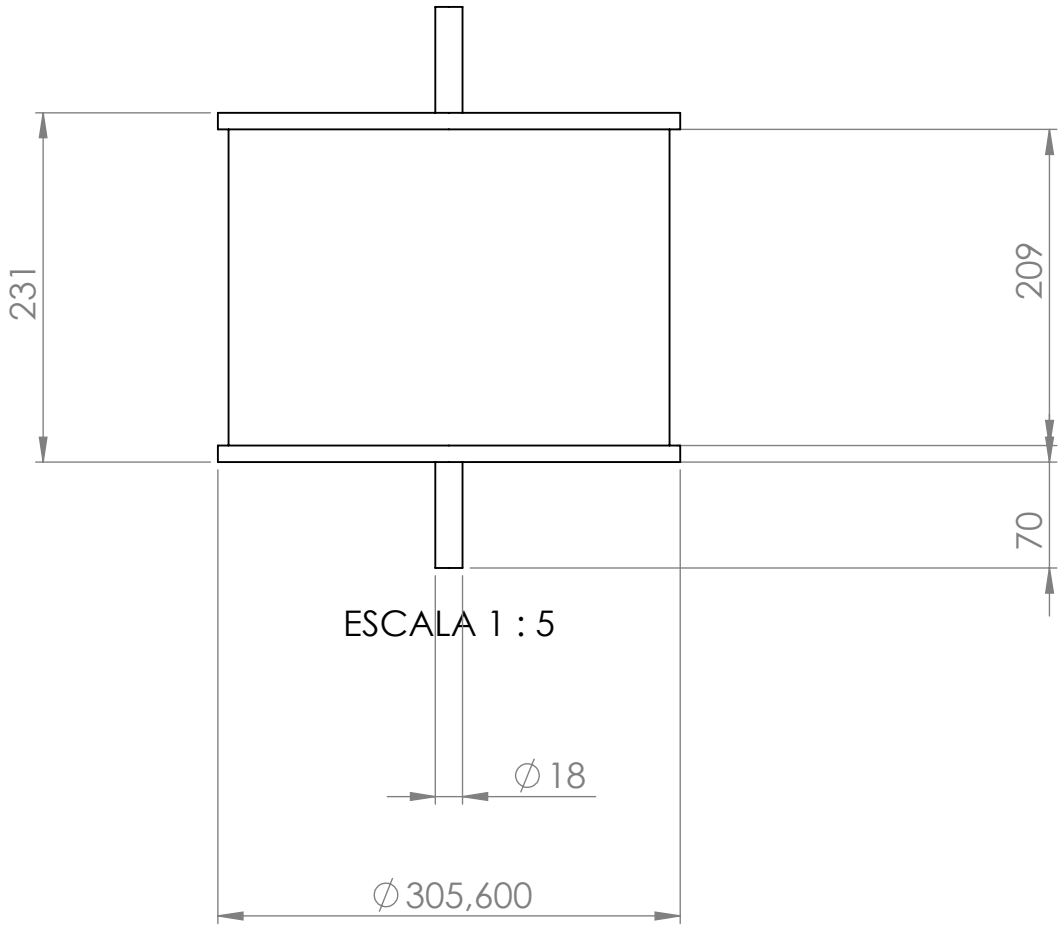

SI NO SE INDICA LO CONTRARIO: LAS COTAS SE EXPRESAN EN MM ACABADO SUPERFICIAL: TOLERANCIAS: LINEAL: ANGULAR:	ACABADO:	REBARBAR Y ROMPER ARISTAS VIVAS	NO CAMBIE LA ESCALA / REVISIÓN

	NOMBRE	FIRMA	FECHA
DIBUJ.			
VERIF.			
APROB.			
FABR.			
CALID.			

MATERIAL:

PESO:

TÍTULO:

Drum

N.º DE DIBUJO

GDSBMD

A4

ESCALA:1:10

HOJA 1 DE 1

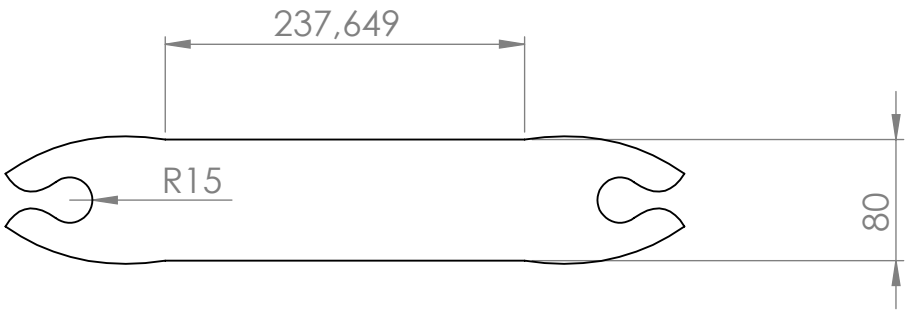

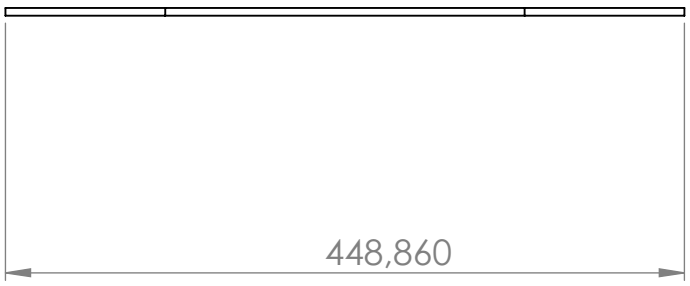

UNLESS OTHERWISE SPECIFIED: DIMENSIONS ARE IN MILLIMETERS SURFACE FINISH: TOLERANCES: LINEAR: ANGULAR:	FINISH:		DEBUR AND BREAK SHARP EDGES	DO NOT SCALE DRAWING	REVISION	
	NAME	SIGNATURE	DATE	TITLE:		
DRAWN				Guideway		
CHK'D						
APPV'D						
MFG						
Q.A				MATERIAL:	DWG NO. GDSBMG	A4
				WEIGHT:	SCALE:1:5	SHEET 1 OF 1

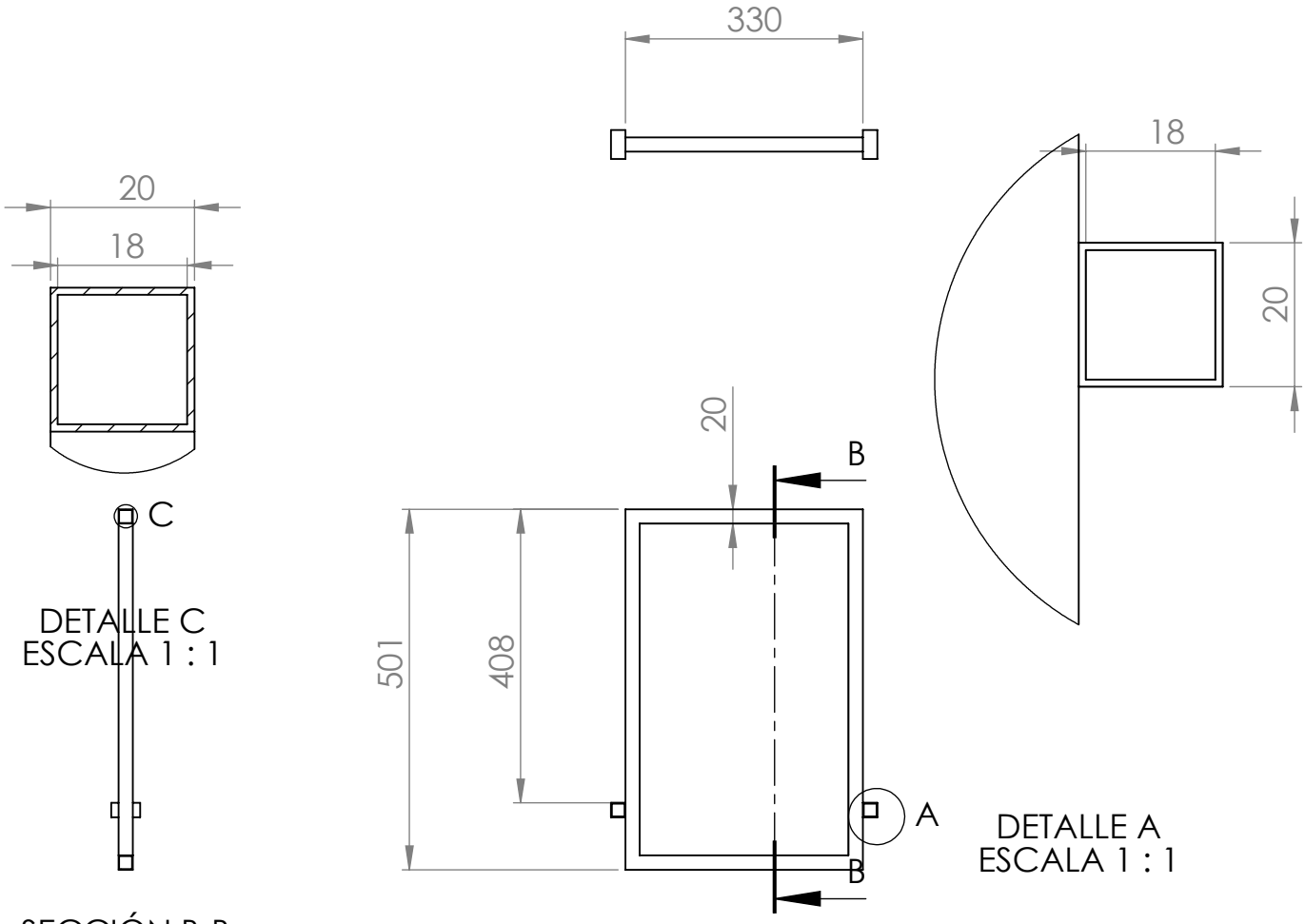

DETALLE C
ESCALA 1 : 1

SECCIÓN B-B

DETALLE A
ESCALA 1 : 1

UNLESS OTHERWISE SPECIFIED: DIMENSIONS ARE IN MILLIMETERS SURFACE FINISH: TOLERANCES: LINEAR: ANGULAR:	FINISH:		DEBUR AND BREAK SHARP EDGES	DO NOT SCALE DRAWING	REVISION	
	NAME	SIGNATURE	DATE	TITLE: Secondary frame		
DRAWN						
CHK'D						
APPV'D						
MFG						
Q.A				MATERIAL:	DWG NO. GDSBMSF	A4
				WEIGHT:	SCALE:1:10	SHEET 1 OF 1

Enclosure 2: Data management

Enclosure 2.1: Set-up of SignalExpress

The set-up of the Signal Express consist of the following steps:

- Selection of the Step Setup menu
- Inside of this menu, Advanced Timing tab is selected
- Inside of this tab, Additional Time Settings is selected
- Inside of the Additional Time Settings option, Timeout is selected, usually 100 seconds
- Selection of Configuration tab
- Inside of latest tab, Samples to Read (kS) and Rate (kHz) are selected to define a sampling time, usually 200 and 2

Enclosure 2.2: Matlab routines

- Collecting data:

  [tama,ancho]=size(medida);

  for i=1:tama

  time(i)=medida(i,1);

  X1(i)=medida(i,2)/.4;

  end

- FFT routine: [tama,ancho]=size(time);

  Fs=(ancho-1)/(time(ancho)-time(1));

  L=ancho;

  NFFT=$2^{nextpow2(L)}$;

  Y=fft(X1,NFFT)/L;

  f=(Fs/2*linspace(0,1,NFFT/2+1));

  plot(f,2*abs(Y(1:NFFT/2+1)))

- Derive routine:

  DT=0.0005;

  for i=2:(ancho-1)

```
medi(i-1)=X1(i); tome(i-1)=time(i);
d(i-1)=(X1(i+1)-X1(i-1))/(2*DT);
end
```